

Abstract

Glaciological and oceanographic observations coupled with numerical models indicate that warm Circumpolar Deep Water (CDW) upwelling onto the West Antarctic continental shelf causes melting of the undersides of floating ice shelves. Because the ice shelves are buttressing glaciers feeding into them, their destabilisation through ocean-induced melting is the predominant driver of current ice loss in Antarctica. Here we present the first data-based reconstruction of Holocene (11,700 years ago to present) variability in CDW inflow to the Amundsen Sea sector, the most vulnerable part of the West Antarctic Ice Sheet. The chemical composition of calcareous foraminifer shells and assemblages of benthic foraminifera in marine sediments indicate that enhanced CDW upwelling, controlled by the latitudinal position of the Southern Hemisphere westerly winds, forced deglaciation of the Amundsen Sea sector both during the early Holocene (11,700 to 7,500 years ago), when an ice-shelf collapse may have caused rapid ice-sheet thinning further upstream, and since the 1940s. These results increase confidence in the predictive capability of current ice-sheet models.

39

40 Today ice discharge from glaciers flowing into the Amundsen Sea Embayment (ASE)
41 (Fig. 1) is the main contributor to the negative mass balance of the West Antarctic ice Sheet
42 (WAIS) and global sea-level rise from Antarctica¹. Rapid thinning, flow acceleration, and
43 grounding-line retreat affecting ice streams and ice shelves in this region have increased since
44 the early 1970s and contributed to global sea-level rise by, on average, $\sim 0.23 \pm 0.02$ mm/yr
45 between 1992 and 2013¹⁻³. Recent modelling suggests that current ice loss of the Thwaites
46 Glacier (Fig. 1), which rests on a bed that is well below sea level and slopes down into the
47 interior of the ASE hinterland, will result in a (partial) WAIS collapse from as early as the 23rd
48 century, thereby raising global sea level over centuries and millennia at rates ≥ 1 mm/yr (ref.4).
49 A similar study predicts that neighbouring Pine Island Glacier, which drains together with
50 Thwaites Glacier into Pine Island Bay (PIB) in the eastern ASE (Fig. 1), will contribute ~ 3.5 -
51 10 mm to eustatic sea-level rise over the next two decades alone¹. Depending on the future
52 extent of atmospheric and oceanic warming, and the dominant processes of ice loss, Antarctica
53 may contribute as much as 1 metre to global sea-level rise by the end of this century⁶.

54 Ocean-driven melting of the undersides of floating ice shelves buttressing the glaciers
55 draining into the ASE has been identified as the main process responsible for the current mass
56 loss. This melting is caused primarily by upwelling of relatively warm Circumpolar Deep
57 Water (CDW) onto the continental shelf⁷⁻¹². Inter-annual to inter-decadal changes in CDW
58 upwelling onto the ASE shelf have been attributed to buoyancy changes⁹ and regional climate
59 variability¹⁰. The latter is assumed to be controlled by latitudinal shifts in the Southern
60 Hemisphere westerly winds (SHWW)¹¹, possibly in response to the Southern Annular Mode¹²
61 and teleconnections to climate in the tropical Pacific¹³.

62 While West Antarctic ice cores provide high-resolution archives of atmospheric
63 changes through the last glacial period to today¹⁴, satellite observations and *in situ*
64 measurements of glaciologic^{2,8} and oceanographic changes^{7,10} are restricted to the last ~ 30 -40
65 years^{4,15}. Until now, no data constrain CDW upwelling onto the ASE shelf prior to this time,
66 and its role in driving centennial to millennial retreat of WAIS remains unclear. This
67 information, however, is crucial for verifying the reliability of the current generation of ice-
68 sheet models which force WAIS deglaciation following the Last Glacial Maximum (LGM; 19-
69 23 kyr BP) predominantly by ocean-induced melting^{16,17} and predict that this process will also
70 drive future Antarctic ice loss in response to global warming^{18,19}, at least during its initial
71 phase⁶. Until now, simulations of ocean forcing have predominantly relied on estimates of
72 deep-water temperatures derived from global climate models that are constrained by far-field
73 oceanic records from outside the Southern Ocean and its complex circulation system^{6,16-18}.

74 Foraminifer shell chemistry and ocean circulation

75 Here we present the first direct evidence for variations in CDW heat supply onto the
 76 ASE shelf during the last 10.4 kyr. We measured the magnesium/calcium (Mg/Ca) ratio of
 77 calcareous shells of the epifaunal to shallow infaunal benthic foraminifer species *Angulogerina*
 78 *angulosa* (Methods) in core PS75/160 recovered just offshore from Pine Island Glacier²¹ (Fig.
 79 1). The Mg/Ca data are used as a proxy for bottom-water temperature²⁰ and thus inflow of
 80 CDW onto the ASE shelf (Methods, see details in Supplementary Information). The low
 81 resolution Mg/Ca record of core PS75/160 is supported by a high-resolution stable carbon
 82 isotope ($\delta^{13}\text{C}$) data set obtained from calcareous shells of *A. angulosa* and the planktic
 83 foraminifer species *Neogloboquadrina pachyderma* sin. from the same site and from site
 84 PS75/167, which is located just offshore from Thwaites Glacier (Fig. 1). We utilize the benthic
 85 $\delta^{13}\text{C}$ ratio as a proxy for the $\delta^{13}\text{C}$ composition of the dissolved inorganic carbon ($\delta^{13}\text{C}_{\text{DIC}}$) of
 86 the ambient seawater and thus, as a tracer for its source water mass. We also measured $\delta^{13}\text{C}$
 87 isotopes on *A. angulosa* in modern sediments from site PS75/215 in PIB and on *N. pachyderma*
 88 sin. in recent sediments from site PS69/251 on the outer ASE shelf^{21,22} (Fig. 1).

89 Foraminiferal $\delta^{13}\text{C}$ records from marine sediments are influenced by water-mass
 90 circulation in addition to vital effects, biological productivity, air-sea exchange of carbon, or a
 91 combination of these factors²³. We corrected the $\delta^{13}\text{C}$ data for species-inherent vital effects as
 92 follows: The $\delta^{13}\text{C}$ signal of *A. angulosa* is known to be on average 0.44-0.60‰ lower than the
 93 $\delta^{13}\text{C}_{\text{DIC}}$ of ambient seawater, but this offset varies regionally²⁴. Mackensen²⁵ analysed the $\delta^{13}\text{C}$
 94 composition of the epibenthic foraminifer genus *Cibicidoides* spp., a reliable recorder of
 95 bottom water $\delta^{13}\text{C}_{\text{DIC}}$, in core-top sediments from site PS2544 on the outer ASE shelf (Fig. 1).
 96 The measured $\delta^{13}\text{C}$ value of +0.63‰ overlaps with the $\delta^{13}\text{C}_{\text{DIC}}$ range of ~-0.3 to 0.6‰ reported
 97 for CDW^{26,27} when the analytical errors for $\delta^{13}\text{C}$ measurements of seawater ($\pm 0.1\text{‰}$) and
 98 foraminiferal calcite ($\pm 0.06\text{‰}$) are taken into account²⁵. In contrast, we measured a $\delta^{13}\text{C}$ ratio
 99 of -0.22‰ on *A. angulosa* from modern sediments at site PS75/215. Because both core sites
 100 are currently bathed by CDW⁷⁻¹¹, we applied an offset correction of +0.85‰ to our benthic
 101 $\delta^{13}\text{C}$ data. Previous studies on *N. pachyderma* sin. shells from south of the Antarctic Polar
 102 Front²⁸ and south of 70°S²⁹, respectively, found a $\delta^{13}\text{C}$ offset of -1.0‰ between the shells and
 103 the ambient surface waters. Accordingly, we corrected our planktic $\delta^{13}\text{C}$ data by adding +1.0‰.

104 To evaluate the influence of past changes in biological productivity on the foraminiferal
 105 $\delta^{13}\text{C}$ down-core record, we measured barium/titanium (Ba/Ti) ratios of cores PS75/160 and
 106 PS75/167 (Fig. 2, Extended Data Fig. 5) as the most reliable palaeoproductivity proxy in
 107 Antarctic continental margin sediments³⁰. Furthermore, we examined the benthic foraminifer

108 assemblages in sediments of core PS75/160 for evidence of environmental changes, especially
109 whether an ice shelf covered PIB from ~12.3-11.2 kyr BP onwards^{31,32}. Ice-shelf cover would
110 have reduced the foraminiferal $\delta^{13}\text{C}$ values by restricting air-sea gas exchange^{25,28}. Cosmogenic
111 isotope surface exposure dates obtained from erratic boulders in the Hudson Mountains near
112 Pine Island Glacier (Fig. 1) suggest that such an ice shelf had buttressed grounded ice upstream
113 from PIB and that its thinning or collapse between 8.3 and 7.5 ka triggered rapid ice-stream
114 thinning by >100 m (ref. 32).

115 Age constraints on cores PS75/160 and PS75/167 are based on previously published^{21,22}
116 and newly calibrated AMS ^{14}C dates on calcareous microfossils (Extended Data Table 1). The
117 recent chronology for core PS69/251, whose modern surface age has been confirmed by core-
118 top AMS ^{14}C dating²¹, is constrained by a lead isotope (^{210}Pb) down-core profile (Extended
119 Data Figs. 2-4, Extended Data Table 2). Core PS75/160, which spans the time period from ~9.2
120 to 1.2 kyr BP (Fig. 2a), was retrieved from a local depression in PIB at a water depth of just
121 337 m. The relatively shallow location of this core explains the abundant occurrence of
122 calcareous microfossils, but another consequence is that the lowermost part of the core, older
123 than ~8.2 kyr BP, is affected by iceberg or ice-shelf keel ploughing²¹. We overcome this issue
124 by splicing the $\delta^{13}\text{C}$ data from core PS75/160 with those from nearby core PS75/167, which
125 span 10.4 to 8.2 kyr BP (Fig. 2b; Extended Data Fig. 1). Core PS75/167 does not contain
126 calcareous microfossils in sediments younger than ~8.2 kyr BP. In the following we refer to
127 the spliced record as the “PIB record”.

128 The benthic Mg/Ca ratios in core PS75/160 imply higher bottom-water temperatures
129 before 7.5 kyr BP, indicating that warm CDW flooded PIB during the early Holocene (11.7-
130 7.5 kyr BP) and that this inflow was reduced during the middle Holocene (7.5-4.0 kyr BP) to
131 late Holocene (4.0-0 kyr BP) (Fig. 3c; Extended Data Fig. 6). Intensified early Holocene CDW
132 inflow is corroborated by both the benthic and the planktic foraminiferal $\delta^{13}\text{C}$ ratios of the PIB
133 record which increase from relatively low values between ~10.4 and 9.0 kyr BP to higher
134 values that are maintained from 7.0 kyr BP until at least 1.2 kyr BP (Figs. 2, 3a,b). The benthic
135 $\delta^{13}\text{C}$ ratios recorded during the early Holocene match the $\delta^{13}\text{C}_{\text{DIC}}$ range of pure CDW. The
136 planktic $\delta^{13}\text{C}$ ratios during this time interval reflect the lower range of $\delta^{13}\text{C}_{\text{DIC}}$ values typical
137 for modern Antarctic Surface Water (AASW)³³ which in the ASE usually forms a 200-300 m
138 thick surface layer^{7,10}. This observation suggests that the reduced $\delta^{13}\text{C}$ ratios of *N. pachyderma*
139 *sin.*, which calcifies within this AASW layer²⁹, are caused by effective admixture of
140 unmodified CDW into AASW.

141 Reduced ^{12}C export to the seabed in PIB caused by a decrease in plankton productivity
 142 can be ruled out as the reason for the benthic foraminifer $\delta^{13}\text{C}$ shift towards heavier values
 143 centred at 7.5 kyr BP because this would have resulted in lighter planktic foraminifer $\delta^{13}\text{C}$
 144 values, i.e. opposite to what is observed. In addition, the Ba/Ti ratios and foraminifer
 145 concentrations in core PS75/160 indicate that biological production probably increased rather
 146 than decreased after ~ 7.5 kyr BP (Fig. 2, Extended Data Fig. 5). An onset or intensification of
 147 air-sea gas exchange between the atmosphere and surface waters in PIB at 7.5 kyr BP might
 148 have resulted from a reduction in ice-shelf coverage. The ice-shelf break-up would be
 149 consistent with the productivity increase after 7.5 kyr BP because phytoplankton production
 150 on the Antarctic continental margin is mainly controlled by the availability of light³⁰. Such a
 151 scenario is in agreement with several early Holocene benthic $\delta^{13}\text{C}$ values in the PIB record that
 152 are even more $\delta^{13}\text{C}$ -depleted than pure CDW as well as a few planktic $\delta^{13}\text{C}$ values that are
 153 lower than $\delta^{13}\text{C}_{\text{DIC}}$ of AASW (Figs. 2, 3a,b). This observed $\delta^{13}\text{C}$ -depletion could be explained
 154 by advection of nearly pure CDW combined with reduced air-sea carbon exchange caused by
 155 ice-shelf cover of PIB during the early Holocene (cf. refs. 31, 32).

156 **Environmental implications from foraminifer assemblages**

157 The benthic foraminifer assemblage in core PS75/160 shows a distinct change at ~ 7.5
 158 kyr BP, when an assemblage dominated by *Nonionella bradii* and *Globocassidulina* species
 159 (*G. subglobosa*, *G. biora*) is replaced by an assemblage dominated by various *Angulogerina*
 160 species, especially *A. angulosa* (Methods), and when both total foraminifer concentration and
 161 arenaceous benthic foraminifer abundance increase (Fig. 2a, Extended Data Fig. 7). While both
 162 *Globocassidulina* species and *Angulogerina* species have been found in modern^{34,35} and
 163 Holocene sub-ice shelf settings³⁶⁻³⁹, an assemblage dominated by *Angulogerina* observed on
 164 the eastern Antarctic Peninsula shelf has been attributed to an ice-shelf edge setting³⁴. Also
 165 *Nonionella* spp. has been reported from modern^{34,35} and Holocene sub-ice shelf sediments^{36,39}
 166 but its dominance in benthic foraminifer assemblages is frequently related to high biological
 167 productivity⁴⁰. Given that neither the benthic $\delta^{13}\text{C}$ values nor the Ba/Ti ratios indicate higher
 168 productivity during the early Holocene (Figs. 2, 3a), we interpret the *Globocassidulina* and
 169 *Nonionella* dominated assemblage to indicate ice-shelf presence. Our interpretation is
 170 consistent with the dominance of *Nonionella* species and *Globocassidulina* species in benthic
 171 foraminifer assemblages of early to late Holocene sediments from the part of the eastern
 172 Antarctic Peninsula shelf which had been permanently ice-shelf covered from 11.5 kyr BP until
 173 AD 2002 (refs. 36, 41).

174 We suggest that PIB remained covered by an extensive ice shelf from at least ~9.2 until
175 ~7.5 kyr BP. This conclusion agrees with the high proportion of a distinct non-encrusted shell
176 morphotype of *N. pachyderma* sin. in the early Holocene sediments of core PS75/160 (Fig. 2a),
177 which is indicative of specimens of a ‘neanic’ (i.e. adolescent) to adult life stage⁴² (Extended
178 Data Fig. 8). In contrast, the middle and late Holocene sediments in core PS75/160 are
179 dominated by an encrusted shell morphotype that is typical for a terminal life stage⁴² (Extended
180 Data Fig. 8). We explain the dominance of the adolescent and adult shells by foraminifer
181 reproduction in seasonal open water offshore from the ice shelf covering PIB, the subsequent
182 advection of these foraminifera under the ice shelf by ocean currents, and their demise in this
183 inhospitable environment for zooplankton, i.e. before they could reach the terminal life stage.
184 A contributing factor for the observed down-core change in the abundance of the two
185 morphotypes of *N. pachyderma* sin. may be a deepening of the pycnocline. Under ice shelves
186 the pycnocline lies deeper than in open water^{7,10} and is overlain by a cool mixed layer, in which
187 non-encrusted morphotypes are concentrated⁴². Given the modern water depth of 337 m at site
188 PS75/160 and taking into account the 30-10 m lower global sea level⁴³ and the predicted ~50
189 m of seafloor depression in response to glacial loading of the PIB hinterland between 10 and
190 7.5 kyr BP⁴⁴, the thickness of this early Holocene ice shelf cannot have exceeded ~410-430 m,
191 which is comparable to the modern thicknesses of Thwaites Glacier Ice Shelf, Ronne Ice Shelf
192 (West Antarctica) and Amery Ice Shelf (East Antarctica) near their calving fronts^{8,45}.

193 Ice-shelf cover of PIB during the early Holocene would have contributed to the low
194 benthic and planktic $\delta^{13}\text{C}$ values recorded during that time. However, bottom-water
195 temperatures under ice shelves are lower than in seasonal open-marine settings^{10,45}, whereas
196 the benthic Mg/Ca data from PIB imply that these temperatures were higher in the proposed
197 early Holocene sub-ice shelf environment than in the middle to late Holocene open-marine
198 setting. Consequently, enhanced CDW supply onto the ASE shelf must have been the dominant
199 factor influencing the early Holocene $\delta^{13}\text{C}$ record from PIB, even if ice-shelf cover contributed
200 to low benthic and planktic $\delta^{13}\text{C}$ values. The most plausible scenario for explaining the
201 simultaneous change in both the foraminiferal $\delta^{13}\text{C}$ composition and the bottom-water
202 temperature around ~7.5 kyr BP is the reduction of CDW inflow. We conclude that compared
203 to the present-day CDW advection onto the ASE shelf, which can be evaluated from the modern
204 benthic and planktic $\delta^{13}\text{C}$ ratios, CDW inflow was stronger from 10.4 to 8.0 kyr BP, while it
205 was weaker from 7.5 to 1.2 kyr BP (Figs. 2, 3a,b).

206 Drivers of ice-sheet change

207 The early Holocene intensification of CDW heat supply can be attributed to a southerly
208 position of the SHWW belt between 12.0 and 8.0 kyr BP⁴⁶ (Fig. 3g,h). The northward shift of
209 the westerlies from 8.0 to 6.0 kyr BP⁴⁶ is likely to have reduced CDW inflow as documented
210 in the PIB record (Fig. 3g,h). Thus, our findings expand on the conclusion from modern
211 observational and modelling studies that the SHWW exert a major control on CDW advection
212 onto the ASE shelf^{7,10,11,15}. The role of buoyancy forcing⁹, however, remains unclear from our
213 data. Early Holocene CDW advection may have been intensified along the entire Pacific
214 margin of West Antarctica and thus may also explain the higher sea-surface temperatures
215 observed on the western Antarctic Peninsula shelf during that time^{40,47} (Fig. 3e).

216 Grounded ice in PIB had retreated to within 110 km of its modern grounding line by
217 11.2 kyr BP^{21,22}. Our conclusion of intensified CDW upwelling onto the ASE shelf from 10.4
218 to 7.5 kyr BP and probably since 12.0 kyr BP, when the SHWW already had a southerly
219 position⁴⁶, suggests that, in accordance with results from ice-sheet modeling¹⁶⁻¹⁹, ocean thermal
220 forcing was the main driver of post-LGM WAIS retreat. In contrast, air temperatures in West
221 Antarctica¹⁴ were still relatively low and post-glacial eustatic sea level had risen by not more
222 than ~60 metres above its LGM low stand of 120 metres^{43,50} when PIB was already free of
223 grounded ice, indicating that atmospheric and sea-level forcing played only a subordinate role
224 for post-LGM WAIS deglaciation (Fig. 3d,f). Sustained high CDW heat supply and
225 accompanying oceanic melting might have destabilised any extensive ice shelf remaining in
226 PIB until 7.5 kyr BP so that afterwards minor atmospheric warming in West Antarctica
227 combined with continued global sea-level rise were sufficient to trigger its disintegration (Fig.
228 3d-f).

229 The modern benthic and planktic $\delta^{13}\text{C}$ ratios indicate that CDW inflow onto the ASE
230 shelf must have increased at some time within the last millennium (Fig. 3a,b). The planktic
231 $\delta^{13}\text{C}$ down-core record available from site PS69/251 on the outer ASE shelf, dating back to AD
232 1888 ± 37 according to its ²¹⁰Pb chronology, reveals that this intensification took place between
233 AD 1947 ± 9 and AD 1963 ± 9 (Fig. 4a). The increased CDW advection can be attributed to a
234 strengthening and/or poleward shift of the SHWW, which is evident from proxy data in West
235 Antarctic ice cores^{48,49} (Fig. 4b,c). Our finding is also in line with the hypothesis that sea-
236 surface temperature warming in the central tropical Pacific Ocean during the 1940s, associated
237 with a very large El Niño event from AD 1939 to 1942, initiated the current period of CDW
238 inflow onto the ASE shelf and the resulting mass loss in this sector of the WAIS¹². This ice
239 loss was not evident until the 1970s, when the first satellite observational data from the ASE
240 sector became available².

241 **Importance**

242 Our study extends the observational record of CDW inflow onto the ASE shelf further
243 back in time through a period of significant ice-sheet change and it suggests early Holocene
244 ice-shelf coverage in PIB. Most significantly, it provides the first empirical evidence for the
245 dominant role of ocean forcing in driving past and recent WAIS deglaciation and the suggested
246 control of CDW upwelling onto the ASE shelf by the SHWW. This information is crucial for
247 validating assumptions in numerical models^{6,18,19} and will help to make model-based
248 predictions of future global sea-level rise from Antarctic ice-sheet melting more robust.

249

250 **Online content** Methods, along with any additional Extended Data display items and Source
251 Data, are available in the online version of the paper; references unique to these sections appear
252 only in the online paper.

253

254 **References**

- 255 1. Sutterley, T.C. *et al.*, Mass loss of the Amundsen Sea Embayment of West Antarctica
256 from four independent techniques. *Geophys. Res. Lett.* **41**, 8421-8428 (2014).
- 257 2. Mougnot, J., Rignot, E. & Scheuch, B. Sustained increase in ice discharge from the
258 Amundsen Sea Embayment, West Antarctica, from 1973 to 2013. *Geophys. Res. Lett.*
259 **41**, 1576-1584 (2014).
- 260 3. Rignot, E., Mougnot, J., Morlighem, M., Seroussi, H. & Scheuch, B. Widespread, rapid
261 grounding line retreat of Pine Island, Thwaites, Smith, and Kohler glaciers, West
262 Antarctica, from 1992 to 2011. *Geophys. Res. Lett.* **41**, 3502-3509 (2014).
- 263 4. Joughin, I., Smith, B. & Medley, B. Marine ice sheet collapse potentially under way for
264 the Thwaites Glacier basin, West Antarctica. *Science* **344**, 735-738 (2014).
- 265 5. Favier, L. *et al.* Retreat of Pine Island Glacier controlled by marine ice-sheet instability.
266 *Nature Climate Change* **4**, 117-121 (2014).
- 267 6. DeConto, R.M. & Pollard, D. Contribution of Antarctica to past and future sea-level
268 rise. *Nature* **531**, 591-597 (2016).
- 269 7. Jacobs, S.S., Jenkins, A., Giulivi, C.F. & Dutrieux, P. Stronger ocean circulation and
270 increased melting under Pine Island Glacier ice shelf. *Nature Geosci.* **4**, 519-523
271 (2011).

- 272 8. Paolo, F.S., Fricker, H.A. & Padman, L. Volume loss from Antarctic ice shelves is
273 accelerating. *Science* **348**, 327-331 (2015).
- 274 9. Wåhlin, A.K. *et al.* Variability of Warm Deep Water inflow in a submarine trough on
275 the Amundsen Sea shelf. *J. Phys. Oceanography* **43**, 2054-2070 (2013).
- 276 10. Dutrieux, P. *et al.* Strong sensitivity of Pine Island Ice-Shelf melting to climatic
277 variability. *Science* **343**, 174-178 (2014).
- 278 11. Thoma, M., Jenkins, A., Holland, D. & Jacobs, S. Modelling Circumpolar Deep Water
279 intrusions on the Amundsen Sea continental shelf, Antarctica. *Geophys. Res. Lett.* **35**,
280 L18602 (2008).
- 281 12. Steig, E.J., Ding, Q., Battisti, D.S. & Jenkins, A. Tropical forcing of Circumpolar Deep
282 Water inflow and outlet glacier thinning in the Amundsen Sea Embayment, West
283 Antarctica. *Annals Glaciol.* **53**, 19-28 (2012).
- 284 13. Ding, Q., Steig, E.J., Battisti, D.S. & Küttel, M. Winter warming in West Antarctica
285 caused by central tropical Pacific warming. *Nature Geosci.* **4**, 398-403 (2011).
- 286 14. WAIS Divide Project Members. Onset of deglacial warming in West Antarctica driven
287 by local orbital forcing. *Nature* **500**, 440-444 (2013).
- 288 15. Schmidtko, S., Heywood, K.J., Thompson, A.F. & Aoki, S. Multidecadal warming of
289 Antarctic waters. *Science* **346**, 1227-1231 (2014).
- 290 16. Pollard, D. & DeConto, R.M. Modelling West Antarctic ice sheet growth and collapse
291 through the past five million years. *Nature* **458**, 329-333 (2009).
- 292 17. Golledge, N.R. *et al.* Antarctic contribution to meltwater pulse 1A from reduced
293 Southern Ocean overturning. *Nature Communications* **5**: **5107**,
294 doi:10.1038/ncomms6107 (2014).
- 295 18. Pollard, D., Chang, W., Haran, M., Applegate, P. & DeConto, R. Large ensemble
296 modeling of the last deglacial retreat of the West Antarctic Ice Sheet: comparison of
297 simple and advanced statistical techniques. *Geosci. Model Dev.* **9**, 1697-1723 (2016).
- 298 19. Golledge, N.R. *et al.* The multi-millennial Antarctic commitment to future sea-level
299 rise. *Nature* **526**, 421-425 (2015).

- 300 20. Katz, M.E. *et al.* Traditional and emerging geochemical proxies in foraminifera. *J.*
301 *Foram. Res.* **40**, 165-192 (2010).
- 302 21. Hillenbrand, C.-D. *et al.* Grounding-line retreat of the West Antarctic Ice Sheet from
303 inner Pine Island Bay. *Geology* **41**, 35-38 (2013).
- 304 22. Larter, R.D. *et al.* Reconstruction of changes in the Amundsen Sea and Bellingshausen
305 Sea sector of the West Antarctic Ice Sheet since the Last Glacial Maximum. *Quat. Sci.*
306 *Rev.* **100**, 55-86 (2014).
- 307 23. Broecker, W.S. & Peng, T.H. *Tracers in the Sea*, 689 pp. (Lamont Doherty Geol. Obs.
308 Publ., Columbia University, New York, 1982).
- 309 24. Mackensen, A. & Licari, L. in *The South Atlantic in the Late Quaternary –*
310 *Reconstruction of Material Budget and Current Systems* (eds. Wefer, G., Mulitza, S. &
311 Ratmeyer, V.), Carbon isotopes of live benthic foraminifera from the eastern South
312 Atlantic Ocean: sensitivity to bottom water carbonate saturation state and organic
313 matter rain rates, pp. 623-644 (Springer, Berlin-Heidelberg, 2004).
- 314 25. Mackensen, A. Strong thermodynamic imprint on Recent bottom-water and epibenthic
315 $\delta^{13}\text{C}$ in the Weddell Sea revealed: Implications for glacial Southern Ocean ventilation.
316 *Earth Planet. Sci. Lett.* **317-318**, 20-26 (2012).
- 317 26. Mackensen, A., Rudolph, M. & Kuhn, G. Late Pleistocene deep-water circulation in the
318 subantarctic eastern Atlantic. *Global Planet. Change* **30**, 197-229 (2001).
- 319 27. Hodell, D.A., Venz, K.A., Charles, C.D. & Ninnemann, U.S. Pleistocene vertical
320 carbon isotope and carbonate gradients in the South Atlantic sector of the Southern
321 Ocean. *Geochem. Geophys. Geosyst.* **4**, 1004, doi:10.1029/2002GC000367 (2003).
- 322 28. Charles, C.D. & Fairbanks, R.A. in *The geological history of the polar oceans: Arctic*
323 *versus Antarctic* (eds. Bleil, U. & Thiede, J.), Glacial to interglacial changes in the
324 isotopic gradients of Southern Ocean surface water, pp. 519-538 (Kluwer Academic,
325 Norwell MA, 1990).
- 326 29. Kohfeld, K.E., Anderson, R.F. & Lynch-Stieglitz, J. Carbon isotopic disequilibrium in
327 polar planktonic foraminifera and its impact on modern and Last Glacial Maximum
328 reconstructions. *Paleoceanography* **15**, 53-64 (2000).

- 329 30. Bonn, W., Gingele, F.X., Grobe, H., Mackensen, A. & Fütterer, D.K.
330 Palaeoproductivity at the Antarctic continental margin: opal and barium records for the
331 last 400 ka. *Palaeogeogr. Palaeoclimatol. Palaeoecol.* **139**, 195-211 (1998).
- 332 31. Kirshner, A.E. *et al.* Post-LGM deglaciation in Pine Island Bay, West Antarctica. *Quat.*
333 *Sci. Rev.* **38**, 11-26 (2012).
- 334 32. Johnson, J.S. *et al.* Rapid thinning of Pine Island Glacier in the Early Holocene. *Science*
335 **343**, 999-1001 (2014).
- 336 33. Mackensen, A. Oxygen and carbon stable isotope tracers of Weddell Sea water masses:
337 new data and some paleoceanographic implications. *Deep-Sea Res. I* **48**, 1401-1422
338 (2001).
- 339 34. Ishman, S.E. & Szymcek, P. Foraminiferal distributions in the former Larsen-A Ice
340 Shelf and Prince Gustav Channel region, eastern Antarctic Peninsula margin: A
341 baseline for Holocene paleoenvironmental change. *Antarctic Res. Ser.* **79**, 239-260
342 (2003).
- 343 35. Barrett, P.J. *et al.*, Oceanography and sedimentation beneath the McMurdo Ice Shelf in
344 Windless Bight, Antarctica, *Antarctic Data Series* **25**, 95 pp. (2007).
- 345 36. Ishman, S.E. *et al.* in *Online Proceedings of the 10th ISAES X* (eds. A.K. Cooper, C.R.
346 Raymond *et al.*), Stable isotopic and foraminiferal evidence of Larsen-B Ice Shelf
347 stability throughout the Holocene. *USGS Open-File Rep.* **2007-1047**, Ext. Abstr. 018,
348 4 pp. (2007).
- 349 37. Pudsey, C.J., Murray, J.W., Appleby, P. & Evans, J. Ice shelf history from petrographic
350 and foraminiferal evidence, Northeast Antarctic Peninsula. *Quat. Sci. Rev.* **25**, 2357-
351 2379 (2006).
- 352 38. Melis, R. & Salvi, G. Late Quaternary foraminiferal assemblages from western Ross
353 Sea (Antarctica) in relation to the main glacial and marine lithofacies. *Marine Micropal.*
354 **70**, 39-53 (2009).
- 355 39. Kilfeather, A.A. *et al.* Ice-stream retreat and ice-shelf history in Marguerite Trough,
356 Antarctic Peninsula: Sedimentological and foraminiferal signatures. *Geol. Soc. Am.*
357 *Bull.* **123**, 997-1015 (2011).

- 358 40. Peck, V.L., Allen, C.S., Kender, S., McClymont, E.L. & Hodgson, D.A. Oceanographic
359 variability on the West Antarctic Peninsula during the Holocene and the influence of
360 upper circumpolar deep water. *Quat. Sci. Rev.* **119**, 54-65 (2015).
- 361 41. Domack, E. *et al.* Stability of the Larsen B ice shelf on the Antarctic Peninsula during
362 the Holocene epoch. *Nature* **436**, 681-685 (2005).
- 363 42. Berberich, D. Die planktische Foraminifere *Neogloboquadrina pachyderma*
364 (Ehrenberg) im Weddellmeer. *Antarktis, Repts. Polar Res.* **195**, 193 pp. (1996).
- 365 43. Blanchon, P., Eisenhauer, A., Fietzke, J. & Liebetrau, V. Rapid sea-level rise and reef
366 back-stepping at the close of the last interglacial highstand. *Nature* **458**, 881-884
367 (2009).
- 368 44. Whitehouse, P.L., Bentley, M.J., Milne, G.A., King, M.A. & Thomas, I.D. A new
369 glacial isostatic adjustment model for Antarctica: calibrated and tested using
370 observations of relative sea-level change and present-day uplift rates. *Geophys. J. Int.*
371 **190**, 1464-1482 (2012).
- 372 45. Nicholls, K.W., Makinson, K. & Østerhus, S. Circulation and water masses beneath the
373 northern Ronne Ice Shelf, Antarctica. *J. Geophys. Res.* **109**, C12017 (2004).
- 374 46. McGlone, M.S., Turney, C.S.M., Wilmshurst, J.M., Renwick, J. & Pahnke, K.
375 Divergent trends in land and ocean temperature in the Southern Ocean over the past
376 18,000 years. *Nature Geosci.* **3**, 622-626 (2010).
- 377 47. Shevennell, A.E., Ingalls, A.E., Domack, E.W. & Kelly, C. Holocene Southern Ocean
378 surface temperature variability west of the Antarctic Peninsula. *Nature* **470**, 250-254
379 (2011).
- 380 48. Koffman, B.G. *et al.* Centennial-scale variability of the Southern Hemisphere westerly
381 wind belt in the eastern Pacific over the past two millennia. *Clim. Past* **10**, 1125-1144
382 (2014).
- 383 49. Dixon, D.A. *et al.* An ice-core proxy for northerly air mass incursions into West
384 Antarctica. *Int. J. Climatol.* **32**, 1455-1465 (2012).
- 385 50. Toscano, M.A., Peltier, W.R. & Drummond, R. ICE-5G and ICE-6G models of
386 postglacial relative sea-level history applied to the Holocene coral reef record of

387 northeastern St Croix, U.S.V.I.: Investigating the influence of rotational feedback on
388 GIA processes at tropical latitudes. *Quat. Sci. Rev.* **30**, 3032-3042 (2011).

389

390 **Supplementary Information** is available in the online version of the paper.

391

392 **Acknowledgements**

393 This study is part of the Polar Science for Planet Earth Programme of the British Antarctic
394 Survey and the PACES II (Polar Regions and Coasts in the changing Earth System) programme
395 of the Alfred-Wegener-Institut. It was funded by the Natural Environment Research Council
396 (NERC), NERC grant NE/M013081/1 and the Helmholtz Association. This work was also
397 funded (in part) by The European Research Council (ERC grant 2010-NEWLOG ADG-267931
398 HE). The data reported in this paper are archived in the PANGAEA database under
399 doi:10.1594/PANGAEA.XXX [*number to be assigned after acceptance*]. We thank the
400 captain, crew, shipboard scientists and support staff participating in R/V *Polarstern* expeditions
401 ANT-XXIII/4 and ANT-XXVI/3, and are grateful to R. Downey, T. Williams, V. Peck, H.
402 Blagbrough, R. Fröhlking and S. Wiebe for their assistance. Furthermore, we thank three
403 anonymous referees for their thoughtful comments which helped to improve the paper.

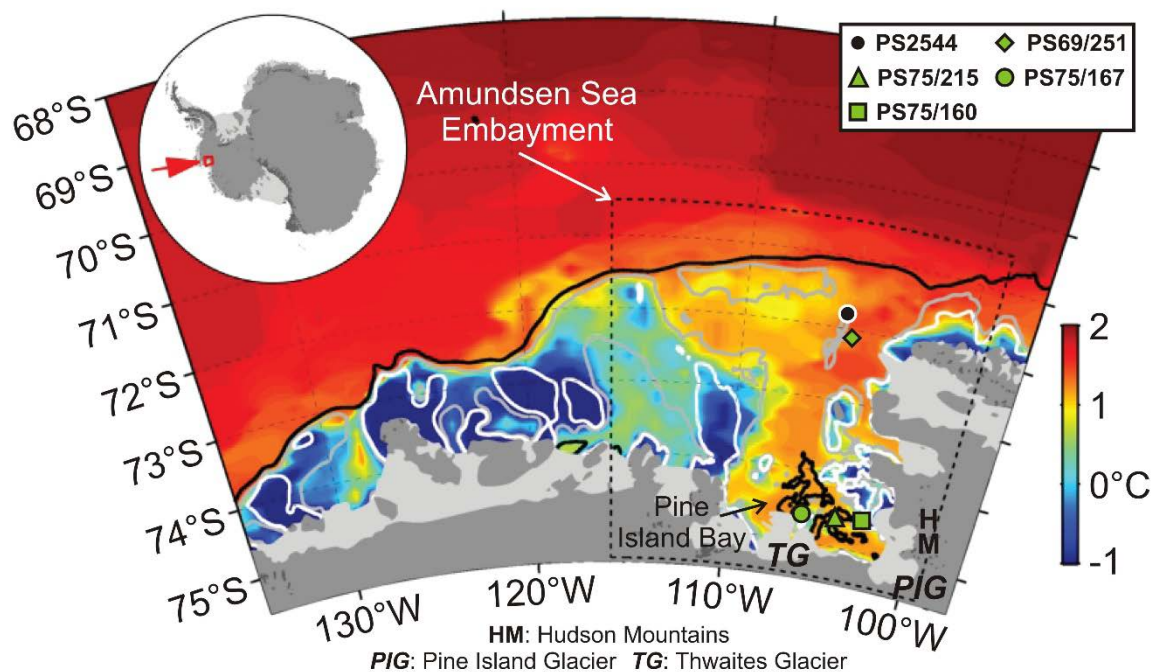
404

405 **Author contributions** CDH conceived the idea for the study and together with JAS, GK and
406 RDL wrote the manuscript. GK, CDH and KG collected the PS69 sediment core and together
407 with JAS, PEJ and JPK the PS75 cores. CDH, JAS, SJR and RDL developed the ^{14}C age models
408 for the PS75 cores. TJA conducted the ^{210}Pb measurements on the PS69 core and provided its
409 age model. GK, CDH, JAS, JPK and PEJ undertook the sedimentological analyses. DH
410 measured stable isotopes on the foraminifer shells, while MG and HE analysed the trace metals.
411 CJP, SK and MW analysed the foraminifer assemblages. All co-authors commented on the
412 manuscript and provided input to its final version.

413

414 **Author Information** The data are available from the PANGAEA data base (PANGAEA doi
415 in preparation) and Extended Data Table 1. Reprints and permissions information is available
416 at www.nature.com/reprints. The authors declare no competing financial interests. Readers are
417 welcome to comment on the online version of the paper. Correspondence and requests for
418 materials should be addressed to CDH (hilc@bas.ac.uk).

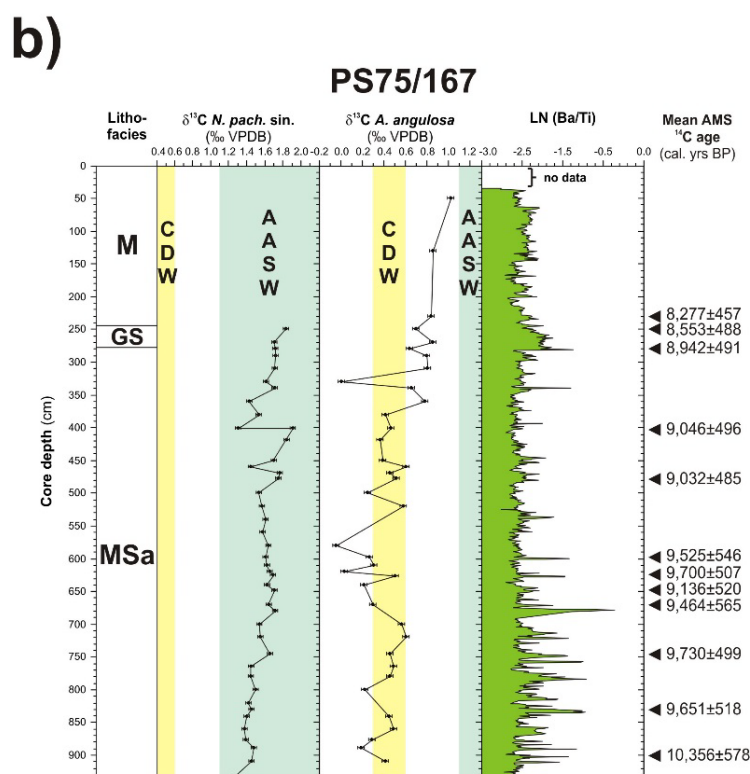
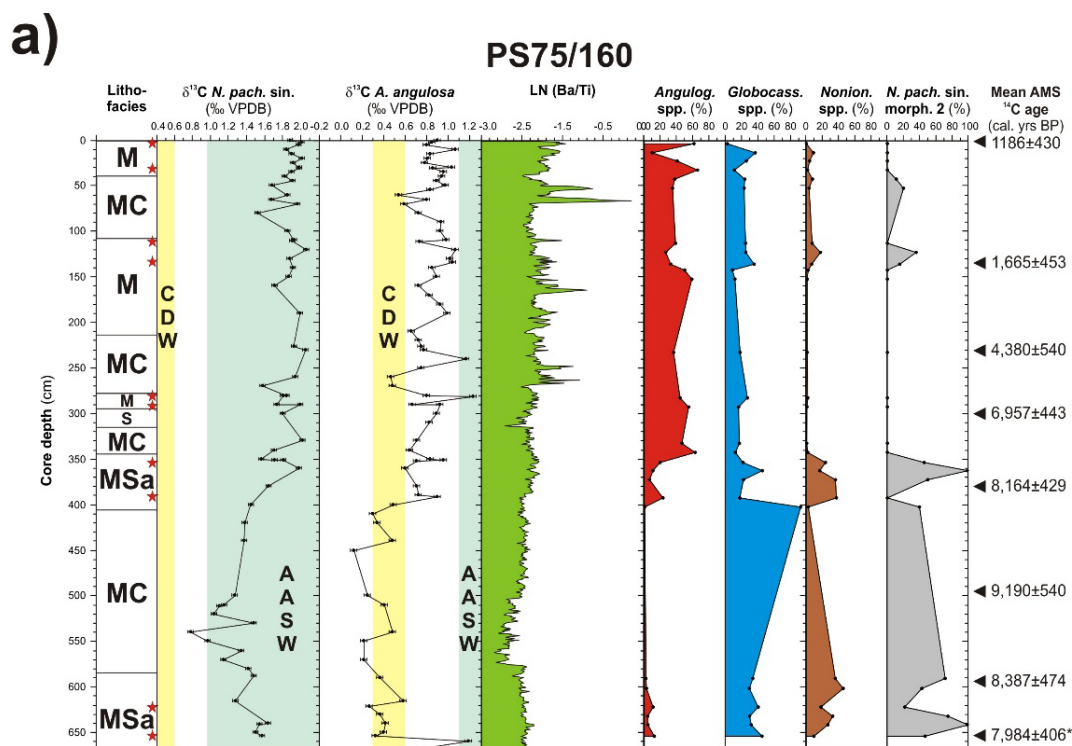
419

420 **Figures:**

421

422 **Fig. 1: Map of modern bottom-water temperatures in the southern Amundsen Sea**
 423 **showing geographical locations and core sites (modified from Dutrieux et al.¹⁰).** Green
 424 symbols indicate locations of cores analysed in this study, while the black symbol marks the
 425 site of a seafloor surface sample investigated for benthic foraminifer $\delta^{13}C$ on *Cibicidoides* spp.
 426 by Mackensen²⁵. Thick black, gray and white contours indicate seabed elevations of -1000 m,
 427 -500 m and -400 m, respectively (for a detailed bathymetric map of inner Pine Island Bay see
 428 Fig. 6 in Larter et al.²²).

429

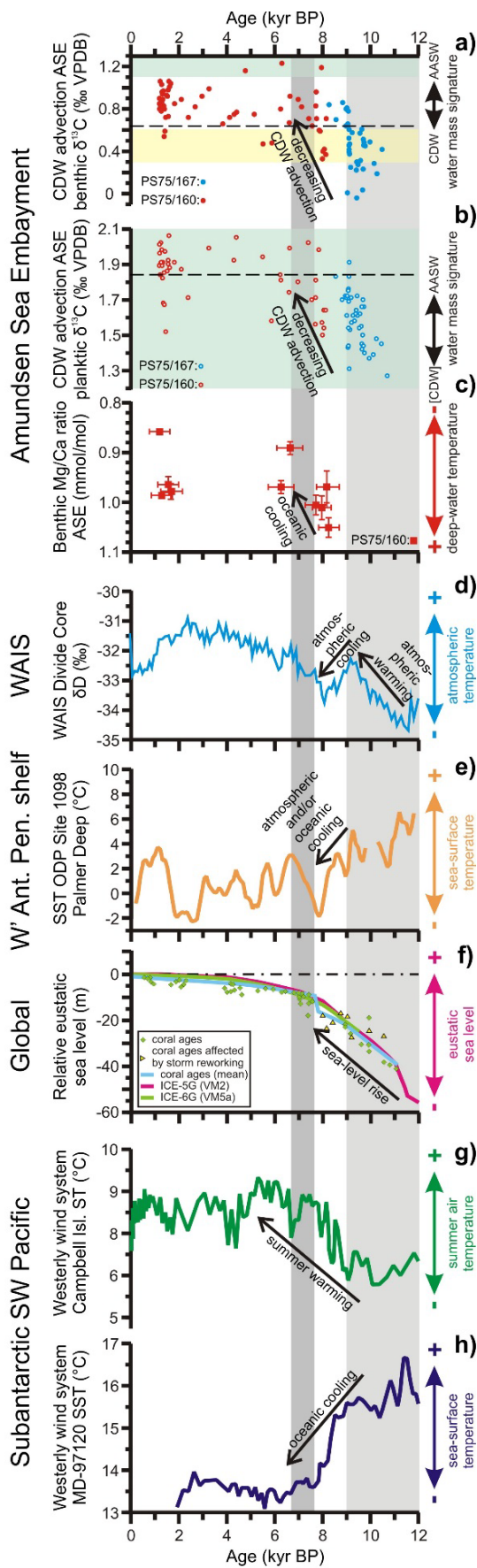


430

431 **Fig. 2: Down-core variability of lithological facies, stable carbon isotope ($\delta^{13}\text{C}$)**
 432 **composition of foraminifer shells, biological productivity and benthic foraminifer**
 433 **assemblages (core PS75/160 only) alongside mean radiocarbon dates for Holocene marine**
 434 **sediment cores PS75/160 (Fig. 2a) and PS75/167 (Fig. 2b) from Pine Island Bay (PIB).**

435 Lithofacies is from Hillenbrand et al.²¹ (M: bioturbated mud; MC: deformed, sheared pebble-
436 sized muddy to sandy soft sediment clasts randomly orientated in muddy matrix; MSa: mud
437 interstratified with sandy layers; S: slightly bioturbated sand; GS: massive sandy gravel).
438 AMS ¹⁴C dates were recalibrated for this study (Extended Data Table 1). Asterisk at lowermost
439 age from core PS75/160 indicates average of replicate dates from the same sample horizon.
440 Facies MC at site PS75/160 probably results from seafloor scouring by iceberg or ice-shelf
441 keels²¹ but AMS ¹⁴C dates indicate reworking only for depth below 405 cm. $\delta^{13}\text{C}$ composition
442 of planktic (*Neogloboquadrina pachyderma* sinistral) and benthic (*Angulogerina angulosa*)
443 foraminifera and log-normalised Ba/Ti peak area ratios are shown for both cores.. The yellow
444 shaded areas highlight the range of $\delta^{13}\text{C}_{\text{DIC}}$ values typical for Circumpolar Deep Water
445 (CDW)^{26,27}, while the blue-green shaded areas indicate the $\delta^{13}\text{C}_{\text{DIC}}$ range typical for Antarctic
446 Surface Water (AASW)³³. Abundances of the three main benthic foraminifera groups
447 (*Angulogerina* spp., *Globocassidulina* spp., *Nonionella* spp.) among all benthic foraminifera
448 and of morphotype 2 tests among all planktic foraminifera tests of *Neogloboquadrina*
449 *pachyderma* sin. (Extended Data Fig. 8) are displayed for core PS75/160. Red asterisks in
450 lithofacies column of core PS75/160 indicate horizons sampled for Mg/Ca analyses on
451 *Angulogerina angulosa*.

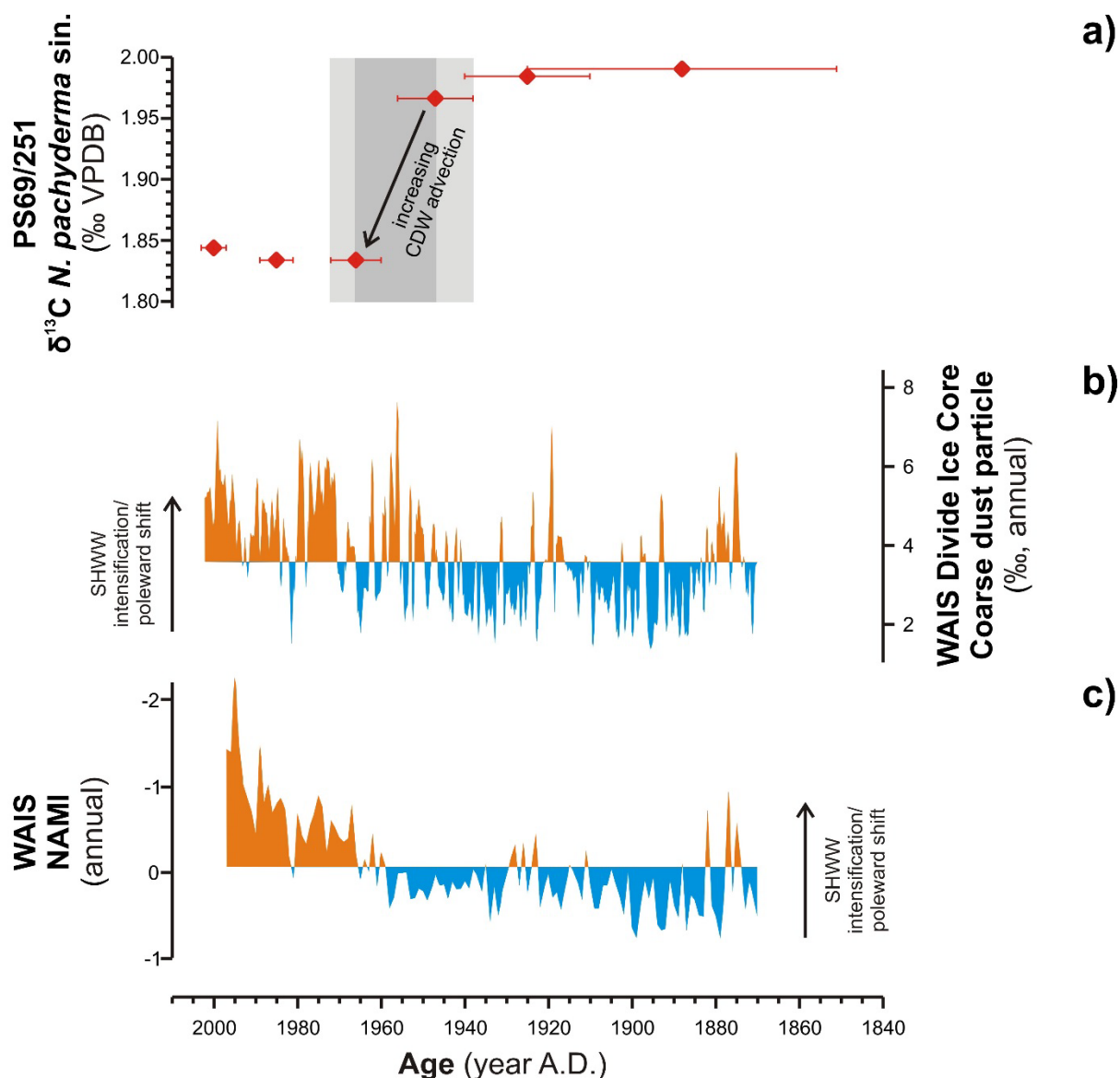
452



454 **Fig. 3: Variability of Circumpolar Deep Water advection onto the Amundsen Sea**
 455 **Embayment shelf since 12 cal. ka BP in comparison to potential forcing mechanisms of**
 456 **ice-sheet change in West Antarctica.** Panels (a), (b) and (c): Proxies for CDW advection into
 457 PIB. $\delta^{13}\text{C}$ composition of (a) benthic (*A. angulosa*) and (b) planktic foraminifera (*N.*
 458 *pachyderma* sin.) in the spliced PS75/160 and PS75/167 record, with $\delta^{13}\text{C}$ values of modern
 459 benthic (PS75/215) and planktic (PS69/251) foraminifera indicated by the black dashed lines
 460 and $\delta^{13}\text{C}_{\text{DIC}}$ ranges typical for CDW and AASW highlighted by the yellow shaded and blue-
 461 green shaded areas, respectively; (c) Mg/Ca ratios of benthic foraminifera (*A. angulosa*) as a
 462 semi-quantitative proxy for bottom-water temperatures at site PS75/160 (Mg/Ca data corrected
 463 for diagenetic coating of shells using $\text{Mg}/\text{Mn} = 0.15$ mol/mol, see Extended Data Fig. 6 for
 464 details; ages for Mg/Ca data points calculated by linear interpolation between maximum and
 465 minimum calibrated dates of neighbouring AMS ^{14}C samples given in Extended Data Table 1).
 466 Panel (d): Deuterium (δD) isotope ratio in the WAIS Divide Ice Core from central West
 467 Antarctica¹⁴ as proxy for air temperature forcing. Panel (e): Sea water surface temperature
 468 (SST) from ODP Site 1098 in Palmer Deep, western Antarctic Peninsula shelf, as proxy for
 469 combined atmospheric and/or oceanic forcing⁴⁷. Panel (f): Global sea-level curves^{43,50} as
 470 proxies for sea-level forcing. Panels (g) and (h): Atmosphere-ocean temperature gradient in the
 471 Sub-Antarctic SW Pacific as a proxy for the position of the Southern Hemisphere westerly
 472 winds (SHWW)⁴⁶ (increase of temperature gradient indicates its N-ward shift). (g) surface air
 473 temperature (ST) on Campbell Island, (h) SST at core site MD-97120, SW of New Zealand.
 474 Light gray shaded area indicates timing of grounded WAIS retreat from the inner ASE
 475 shelf^{21,22}, dark gray shaded area highlights that the timing of a major decrease in CDW
 476 advection onto the ASE shelf coincided with a N-ward shift of the SHWW.

477

478



479

480 **Fig. 4: Variability of Circumpolar Deep Water advection onto the Amundsen Sea**
 481 **Embayment shelf and Southern Hemisphere westerly winds during the last 150 years.**

482 Panel (a): $\delta^{13}\text{C}$ composition of planktic foraminifer shells in core PS69/251 from the outer ASE
 483 shelf versus age (derived from ^{210}Pb -dating). Error bars of the data points indicate the
 484 uncertainty of the ^{210}Pb ages with the light and dark gray shaded areas illustrating the possible
 485 timing and the most likely timing, respectively, of an increased admixture of CDW into AASW
 486 as indicated by the planktic $\delta^{13}\text{C}$ values. Panel (b): Annual coarse dust particle percentage
 487 (defined as the number of particles mL^{-1} $[4.5\text{--}15]/[1\text{--}15]$ μm diameter $\times 100$) in the WAIS
 488 Divide Ice Core (48). Panel (c): Proxy for “northerly air mass incursions” (NAMI) into West
 489 Antarctica, based on stacked non-sea-salt Ca^{2+} concentration data from 10 ice cores (49). The
 490 orange/blue delineation for the curves in panels (b) and (c) is the mean of that record over the

491 time interval shown. The ice core proxies indicate that intensification and/or poleward shift of
492 the SHWW coincided with increased CDW advection onto the ASE shelf.

Supplementary Online Information

Oceanic forcing of Holocene ice-sheet retreat in the Amundsen Sea Embayment, West Antarctica

Authors: Claus-Dieter Hillenbrand*, James A. Smith, David A. Hodell, Mervyn Greaves, Christopher R. Poole, Sev Kender, Mark Williams, Thorbjørn Joest Andersen, Patrycja E. Jernas, Henry Elderfield, Johann P. Klages, Stephen J. Roberts, Karsten Gohl, Robert D. Larter & Gerhard Kuhn

*Corresponding author. Email: hilc@bas.ac.uk

Content:

- Online Materials and Methods
- Extended Data Figure 1
- Extended Data Figure 2
- Extended Data Figure 3
- Extended Data Figure 4
- Extended Data Figure 5
- Extended Data Figure 6
- Extended Data Figure 7
- Extended Data Figure 8
- Extended Data Table 1
- Extended Data Table 2
- Supplementary References

Methods

Core material. Gravity cores PS75/160-1 and PS75/167-1 and giant box core PS75/215-1 were recovered on RV *Polarstern* expedition ANT-XXVI/3 in 2010 (ref. 51), while giant box core PS69/251-1 was retrieved during RV *Polarstern* expedition ANT-XXIII/4 in 2006 (ref. 52) (Extended Data Table 1). For metadata, detailed core descriptions and X-radiographs of the cores, see Hillenbrand et al.²¹, Larter et al.²², Smith et al.⁵³ and doi.pangaea.de/10.1594/PANGAEA.751493.

Core processing, sedimentological analyses and chronologies. Methodologies of core processing and sedimentological analyses were reported by Hillenbrand et al.²¹, Larter et al.²² and Smith et al.⁵³. Analytical techniques for AMS ¹⁴C dating and calibrated AMS ¹⁴C ages were also previously published^{21,22,53} (see also doi.pangaea.de/10.1594/PANGAEA.751493) but for this study we re-calibrated all conventional AMS ¹⁴C dates from cores PS75/160-1 and PS75/167-1 (Extended Data Table 1). Because mixed calcareous (micro-)fossils, which are known to show variable ¹⁴C vital effects⁴¹, had been radiocarbon-dated from cores PS75/160-1 and PS75/167-1, we used a marine reservoir age with a relatively large error ($R+\Delta R=1,100\pm 200$ years) for their calibration²¹. In contrast, Larter et al.²² and Smith et al.⁵³ applied a uniform marine reservoir age with a much smaller error ($R+\Delta R=1,300\pm 70$ years) to their calibration. Calibration was conducted using the CALIB 7.1 calibration programme⁵⁴ using the MARINE13 (100%) calibration curve⁵⁵.

All reported and calibrated AMS ¹⁴C dates for core PS75/167-1 increase down-core or overlap within error but no ¹⁴C dates are available above 230 cm depth (Fig. 2b; Extended Data Table 1). The ¹⁴C dates for core PS75/160-1 show an age reversal below ~400 cm core depth (Fig. 2a; Extended Data Table 1). A thick unit of a distinct lithofacies (facies MC: deformed, sheared pebble-sized muddy to sandy soft sediment clasts randomly orientated in muddy matrix) occurs at this depth (Fig. 2a) suggesting that this lower part of core PS75/160-1 was affected by post-depositional turbation of the seafloor sediments by iceberg or ice-shelf keels²¹. Rather than ignoring the three trace metal (i.e. Mg/Ca) data and the benthic foraminifer assemblage data obtained from samples taken below this depth, we assigned for those samples ages by linear interpolation between maximum and minimum calibrated AMS ¹⁴C dates of neighbouring age-depth fix points. This approach leaves some uncertainty in the absolute ages for the corresponding samples but an early Holocene age for the lower part of core PS75/160-1 is documented by the available AMS ¹⁴C dates (Fig. 2a; Extended Data Table 1). We spliced the

stable carbon isotope ($\delta^{13}\text{C}$) records of cores PS75/160-1 and PS75/167-1 at 8.2 kyr BP (Extended Data Fig. 1) and used exclusively $\delta^{13}\text{C}$ data from below 230 cm depth in core PS75/167-1 for the time interval >8.2 kyr BP and from above 380 cm depth in core PS75/160-1 for the time span <8.2 kyr BP (Fig. 3a,b).

Radiocarbon dating of planktic foraminifera (*Neogloboquadrina pachyderma* sinistral) from undisturbed seafloor surface sediment retrieved in giant box core PS69/251-1 provided an uncorrected AMS ^{14}C age of $1,144 \pm 37$ years^{21,53} and thus the youngest ^{14}C date obtained from modern surface sediments from the continental shelf in the Amundsen and Bellingshausen seas²² (Extended Data Table 1). As calcareous (micro-)fossil material was insufficient for AMS ^{14}C dating in samples taken from below the surface, lead-210 (^{210}Pb) and caesium-137 (^{137}Cs) dating were applied to core PS69/251-1 for establishing ages of down-core samples. The ^{210}Pb and ^{137}Cs activities were measured on 1 cm thick sediment slices by gamma-spectrometry using Canberra ultra-low-background Ge-detectors at the Gamma Dating Centre, Department of Geosciences and Natural Resource Management, University of Copenhagen. ^{210}Pb was measured from its gamma-peak at 46.5 keV, ^{226}Ra from the granddaughter ^{214}Pb (peaks at 295 and 352 keV) and ^{137}Cs from its peak at 661 keV. The core showed surface contents of unsupported ^{210}Pb of $\sim 115 \text{ Bq kg}^{-1}$ with a tendency for exponential decline with depth in the upper 6 cm (Extended Data Fig. 2). Below ~ 6 cm core depth the activity was at the detection limit or lower. The calculated flux of unsupported ^{210}Pb is $100 \text{ Bq m}^{-2} \text{ yr}^{-1}$ which is in reasonable agreement with the expected flux from atmospheric deposition⁵⁶. The content of ^{137}Cs was generally very low (Extended Data Fig. 2). Constant Rate of Supply (CRS) modelling was applied on the profile using a modified method⁵⁶ where the activity below 5.5 cm was calculated on the basis of a regression (Extended Data Fig. 3). The dating results are given in Extended Data Table 2 and Extended Data Figure 4.

X-ray fluorescence scanning. Semi-quantitative uncalibrated major and trace element composition of cores PS75/160-1 and PS75/167-1 were analysed at the Alfred Wegener Institute (Bremerhaven) using an Avaatech XRF core scanner⁵⁷. We applied XRF core scanning predominantly for the determination of the barium/titanium (Ba/Ti) peak-area ratio (hereafter referred to as the Ba/Ti ratio), which is a proxy for biogenic barium (Ba_{bio}). Ba_{bio} is considered to be the most reliable palaeoproductivity proxy in Antarctic continental margin sediments and Southern Ocean sediments south of the Antarctic Polar Front^{30,58-60}. Following Weltje and Tjallingii⁶¹ we plotted the log-normalised $[\text{Ln}(\text{Ba}/\text{Ti})]$ peak-area ratios in Figures 2 and Extended Data Figure 5. In order to assess down-core changes in the input of barium that is

incorporated in the terrigenous heavy mineral barite we also calculated the log-normalised barium/zirconium (Ba/Zr) peak-area ratios, with Zr being a proxy for the terrigenous heavy mineral zircon (Extended Data Fig. 5).

Stable carbon and oxygen isotope analyses. Stable carbon ($\delta^{13}\text{C}$) and oxygen ($\delta^{18}\text{O}$) isotope analyses were performed on the planktic foraminifer species *Neogloboquadrina pachyderma* sinistral (12-24 shells; morphotype 1) and the epibenthic to shallow infaunal foraminifer *Angulogerina angulosa* (= *Trifarina angulosa*) (5-20 shells) (Extended Data Figs. 5, 7). The $\delta^{13}\text{C}$ and $\delta^{18}\text{O}$ isotopes were measured on 104 planktic and 112 benthic foraminifer samples from cores PS75/160-1 and PS75/167-1, one benthic foraminifer sample from site PS75/215-1 and seven planktic foraminifer samples from core PS69/251-1. The shells were picked from the wet sieved 63-2000 μm sediment size fraction and analysed at the Godwin Laboratory for Palaeoclimate Research at the Department of Earth Sciences, University of Cambridge (UK). Foraminifer shells were first crushed and soaked in a solution of 3% H_2O_2 for 30 minutes, then acetone was added and the sample ultrasonicated for 10 seconds before the liquid was decanted. Samples were then dried at 50°C overnight. Vials were sealed with septa and screw caps and analysed using a Micromass Multicarb sample preparation system attached to a VG SIRA Mass Spectrometer. Each run of 30 samples was accompanied by ten reference carbonates and two control samples. Results are reported with reference to the international standard Vienna Pee Dee Belemnite (VPDB) and analytical precision is better than $\pm 0.06\text{‰}$ for $\delta^{13}\text{C}$ and $\pm 0.08\text{‰}$ for $\delta^{18}\text{O}$. In this study, we only used the $\delta^{13}\text{C}$ data of *A. angulosa* and *N. pachyderma* sin. The $\delta^{13}\text{C}$ data of *A. angulosa* and *N. pachyderma* sin. were corrected for vital effects by adding $+0.85\text{‰}$ (cf. ref. 24) and $+1.0\text{‰}$ (refs. 28, 29), respectively.

Trace metal analyses. Ten samples from core PS75/160-1 contained sufficient calcareous benthic foraminifer shells of *A. angulosa* (200-300 μg) and ten samples from this core contained sufficient planktic foraminifer shells of *N. pachyderma* sin. (300-500 μg) for trace metal analyses. Samples were only taken from horizons with a lithofacies that does not indicate signs of reworking (i.e. no samples were taken from facies MC; Fig. 2a).

Cleaning of the shells followed the procedure described in Barker et al.⁶². Element ratios were determined by ICP-OES⁶³ and ICP-MS⁶⁴. Long-term instrumental precision of element ratio data, determined by replicate analyses of a standard solution containing magnesium/calcium (Mg/Ca)= 1.3 mmol/mol, was $\pm 0.46\%$. Accuracy of Mg/Ca determinations was confirmed by inter-laboratory studies of foraminifer and carbonate reference materials^{65,66}.

Iron/calcium (Fe/Ca) and manganese/calcium (Mn/Ca) were measured to monitor cleaning efficiency and diagenetic effects. The *N. pachyderma* sin. samples contained high Fe/Ca and Mn/Ca (up to 0.40 and 2.48 mmol/mol respectively) with strong positive correlation between Mg/Ca, Fe/Ca ($r^2=0.93$) and Mn/Ca ($r^2=0.94$), reflecting diagenetic coating of the shells⁶⁷ not removed by the cleaning procedure. Therefore, the Mg/Ca data on *N. pachyderma* sin. are not interpreted. The *A. angulosa* samples contained much lower Fe/Ca and Mn/Ca (maximum 0.14 and 0.64 mmol/mol, respectively) with no correlation observed between Mg/Ca and Fe/Ca ($r^2=0.02$) and a smaller (but still significant) correlation between Mg/Ca and Mn/Ca ($r^2=0.56$). In order to evaluate the impact of any diagenetic Mg contribution on the Mg/Ca data, we applied a correction to the measured Mg/Ca of *A. angulosa* (Fig. 3c, Extended Data Fig. 6a), assuming Mg/Mn of a diagenetic coating is 0.15 ± 0.05 mol/mol, reflecting average composition of Mn nodules and ferromanganese crusts^{68,69}, especially of those from the South Pacific and Pacific sector of the Southern Ocean⁷⁰⁻⁷². The adjusted Mg/Ca ratios show the same (although less pronounced) down-core trend as the non-adjusted Mg/Ca data, with higher Mg/Ca ratios found before 7.5 kyr BP (Extended Data Fig. 6a,b). Also use of other Mg/Mn ratios for diagenetic coatings⁶⁹ still indicates that the early to middle Holocene decrease in our Mg/Ca data is a robust feature (Extended Data Fig. 6b).

Boron/Calcium (B/Ca) was analysed on all *A. angulosa* and *N. pachyderma* sin. samples aiming to exclude an influence of alkalinity on the Mg/Ca records^{73,74}. Neither the benthic nor the planktic foraminiferal data show a correlation between Mg/Ca and B/Ca. However, B/Ca values measured on the *A. angulosa* shells were very low, in the range 7.1 to 13.0 $\mu\text{mol/mol}$, and probably influenced by the laboratory blanks. Consequently, the B/Ca data are not interpreted.

The Mg/Ca composition of calcareous foraminifer shells is frequently used as a quantitative proxy for seawater temperature^{20,75} but can also be controlled by the carbonate ion concentration ($[\text{CO}_3^{2-}]$) in the ambient seawater^{73,76}. Consequently, higher Mg/Ca ratios as observed in core PS75/160-1 during the early Holocene (Fig. 3c, Extended Data Fig. 6a) indicate an increase in either the temperatures and/or the $[\text{CO}_3^{2-}]$ of the deep-water mass flooding Pine Island Bay (PIB) during that time. The influence of the latter can be evaluated by measuring the B/Ca ratio of the foraminifer shells^{73,76,77}, which, however, provided only inconclusive results for our samples from core PS75/160-1 (see above). The pre-industrial $[\text{CO}_3^{2-}]$ in Antarctic Surface Water (AASW) was 120 $\mu\text{mol/kg}$ ^{ref.29}, whereas Circumpolar Deep Water (CDW) is characterised by a uniform, relatively low $[\text{CO}_3^{2-}]$ of 84 ± 5 $\mu\text{mol/kg}$ throughout the Southern Ocean, including its Pacific sector and the region south of the Antarctic Polar

Front⁷⁸. If the elevated benthic foraminiferal Mg/Ca ratios in PIB recorded during the early Holocene were caused by the presence of an AASW-like water mass that comprised the entire water column, the corresponding benthic foraminiferal $\delta^{13}\text{C}$ ratios can be expected to resemble $\delta^{13}\text{C}_{\text{DIC}}$ values typical for AASW. In contrast, our early Holocene benthic foraminiferal $\delta^{13}\text{C}$ data from cores PS75/160-1 and PS75/167-1 are lower and typical for CDW (Fig. 3b, Extended Data Fig. 5) and thus not consistent with a scenario that deep water present on the shelf of the Amundsen Sea Embayment (ASE) during that time was derived from AASW with the benthic Mg/Ca data reflecting its higher $[\text{CO}_3^{2-}]$.

Deep-water warming on the ASE shelf could have resulted either from intensified CDW upwelling or CDW warming. CDW warming would have resulted from a higher influx of North Atlantic Deep Water (NADW), which is the source water mass for CDW, into the Southern Ocean. NADW is injected into the clockwise flowing Antarctic Circumpolar Current in the Atlantic sector of the Southern Ocean, mixes with recirculated deep waters from the Indian and Pacific oceans, and, most importantly, acts as the “heat source” for CDW⁷⁹. The $[\text{CO}_3^{2-}]$ of NADW is $\sim 125 \mu\text{mol/kg}$ compared to only $84 \pm 5 \mu\text{mol/kg}$ in CDW⁷⁸. Thus, intensified NADW influx into the Southern Ocean during the early Holocene, which is supported by marine sedimentary records from the Atlantic sector⁸⁰, would have raised both the temperature and the $[\text{CO}_3^{2-}]$ in deep water flooding the ASE shelf, consistent with our Mg/Ca data from PIB. The $\delta^{13}\text{C}_{\text{DIC}}$ of NADW is higher than in CDW⁸¹. Consequently, increased NADW supply would have raised the $\delta^{13}\text{C}_{\text{DIC}}$ of CDW. This, however, is in conflict with the early Holocene benthic foraminiferal $\delta^{13}\text{C}$ data from our PIB cores, which are characterised by low values typical for CDW (Fig. 3b, Extended Data Fig. 5). Consequently, the elevated benthic foraminiferal Mg/Ca ratios recorded in PIB during the early Holocene must reflect deep water warming caused by intensified CDW upwelling.

Analyses of benthic foraminifer assemblages. A total of 38 samples (1 cm thick sediment slices) were taken from core PS75/160-1 for benthic foraminifer analysis⁸². As with the trace metal samples, no samples were taken from the core section with lithofacies MC between ~ 405 and 485 cm depth. The samples were washed through a $63 \mu\text{m}$ mesh-size sieve before the coarse residue was dry-sieved over 2 mm. All samples were screened in order to estimate the abundance of foraminifera. 27 samples with a relatively high content of foraminifera were selected for microscopic analysis and then dry-sieved over $125 \mu\text{m}$ and $250 \mu\text{m}$. 23 of the 27 samples contained >300 benthic foraminifer shells in the $>125 \mu\text{m}$ fraction. Samples with significantly more than 300 specimens and/or a large sample volume were split using a

traditional hand-splitter until a suitable aliquot remained. Picked foraminifera were then identified under an optical microscope and by using Scanning Electron Microscope (SEM) images. Classification and identification were carried out in accordance with literature on recent Antarctic foraminifera (for full reference list, see ref. 82).

Throughout core PS75/160-1, abundances of foraminifera are high, with total numbers ranging from 81 to 1511 specimens per sample, and over 14,000 total specimens were identified from all samples⁸². The 27 samples yielded 84 benthic taxa but only one planktic species (*N. pachyderma* sin.). Between 0 and 341.5 cm core depth the abundance of foraminifera per gram of dry sediment (foraminifera/g) is substantially greater than from 352.5 to 653.5 cm core depth, and there is a large range throughout the core (maximum: 306.19 foraminifera/g at 281.5 cm; minimum: 1.85 foraminifera/g at 631.5 cm) (Extended Data Fig. 7). Between 0 and 341.5 cm core depth, the average concentration of 102.58 foraminifera/g far exceeds the average concentration of only 20.81 foraminifera/g between 352.5 and 653.5 cm core depth.

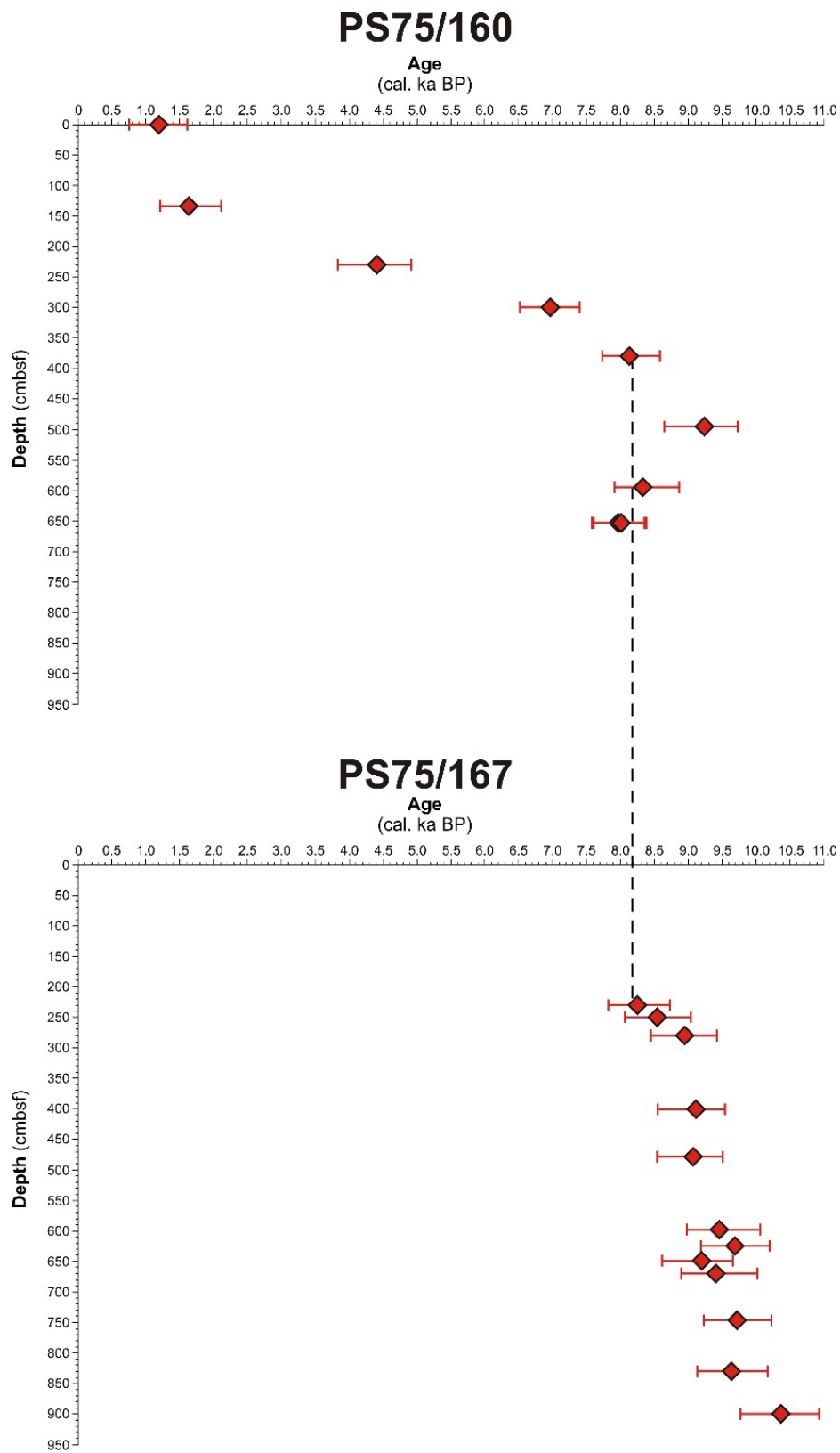
Benthic calcareous species dominate the assemblages throughout the core while the abundance of arenaceous species accounts for a maximum of 30% (depth: 141 cm) (Extended Data Fig. 7). Over two-thirds of samples comprise more than 85% calcareous foraminifera⁸². However, arenaceous foraminifera are more abundant between 0 and 341.5 cm (mean: 15.2%) than between 352.5 and 653.5 cm (mean: 7.0%). *N. pachyderma* sin. is not particularly abundant, contributing a maximum of 5.5% to the total assemblage at 281.5 cm, though it is present in all samples. Preservation of benthic and planktic foraminifer shells was good to moderate throughout the core.

The upper section of core PS75/160-1 from 0 to 341.5 cm depth typically contains high abundances and percentages of the calcareous benthic species *Angulogerina angulosa*, *A. sp. 1*, *Uvigerina sp. 1*, *Globocassidulina subglobosa*, and *G. bitor* (Extended Data Fig. 7). Relatively abundant accessory species include *Astrononion echolsi*, *Alabaminella weddellensis* and the arenaceous species *Miliammina arenacea*, *Portatrochammina sp. 1* and *Labrospira jeffreysii*. We follow previous researchers on benthic foraminifera from the Antarctic continental margin and summarize under 'A. angulosa' the species *A. angulosa*, *A. earlandi*, *Trifarina angulosa* and *T. earlandi*^{37,83-85}, which are morphospecies rather than separate biological species (cf. refs. 86-88). Moreover, molecular genetic data have shown that *Angulogerina/Trifarina* is closely related to *Uvigerina peregrina*^{88,89}, with which it also shares the epifaunal to shallow infaunal habitat^{24,83,90}.

A major faunal change was observed between 341.5 and 352.5 cm core depth. The section below this depth is characterised by low abundances of *A. angulosa* and *A. pauperata*. This

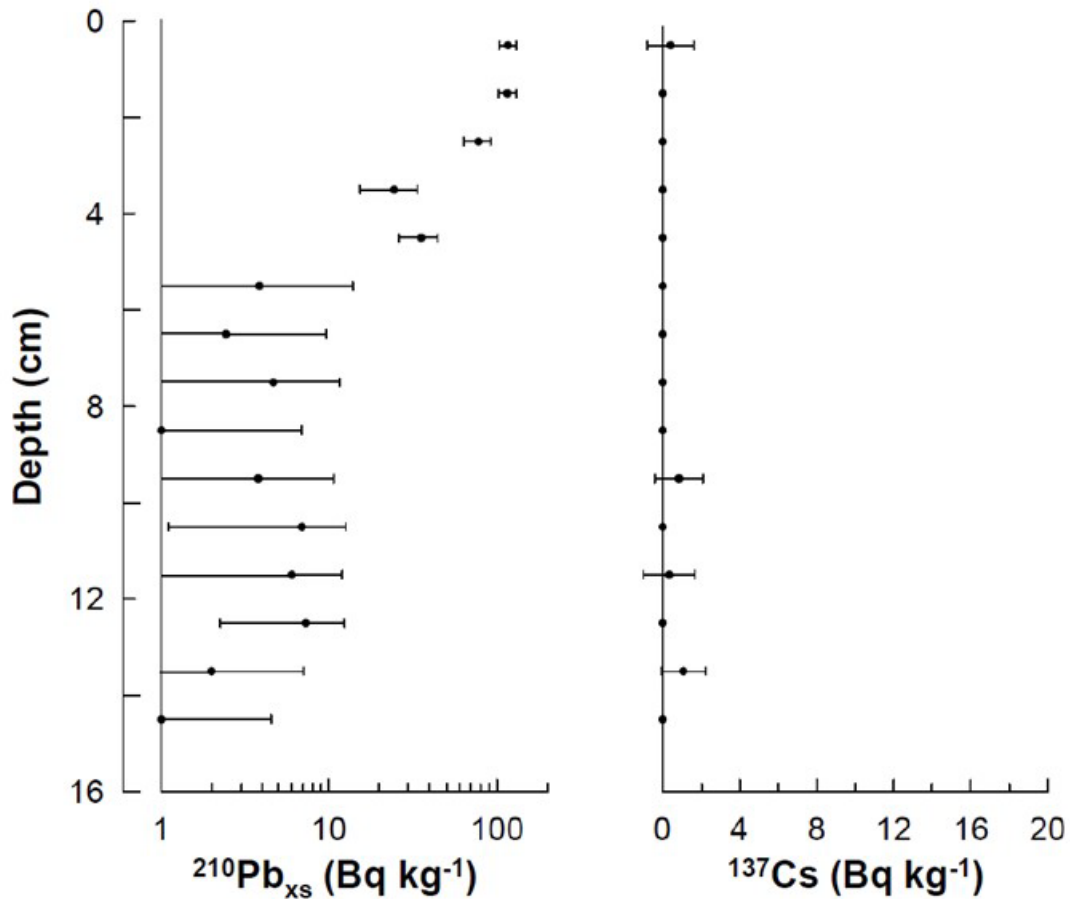
lower core section is dominated by *Nonionella bradii*, *N. iridea*, *G. subglobosa*, and *G. biora* (Extended Data Fig. 7). The subsidiary species include *Ehrenbergina glabra*, *Fursenkoina fusiformis* (calcareous), and *Portatrochammina* sp. 1 (arenaceous). The planktic foraminifera in this lower core section are dominated by *N. pachyderma* sin. type 2, while *N. pachyderma* sin. type 1 dominates the upper section (Extended Data Figs. 7, 8). Principal Component Analysis (PCA), Correspondence Analysis (CA) and Cluster Analysis demonstrate that the pronounced change between the two dominant benthic foraminifera assemblages between 341.5 and 352.5 cm core depth is statistically robust⁸².

Extended Data Figures



Extended Data Figure 1: Age-depth plots for cores PS75/160-1 (above) and PS75/167-1 (below). The red diamonds mark the calibrated median AMS ^{14}C ages with the error bars

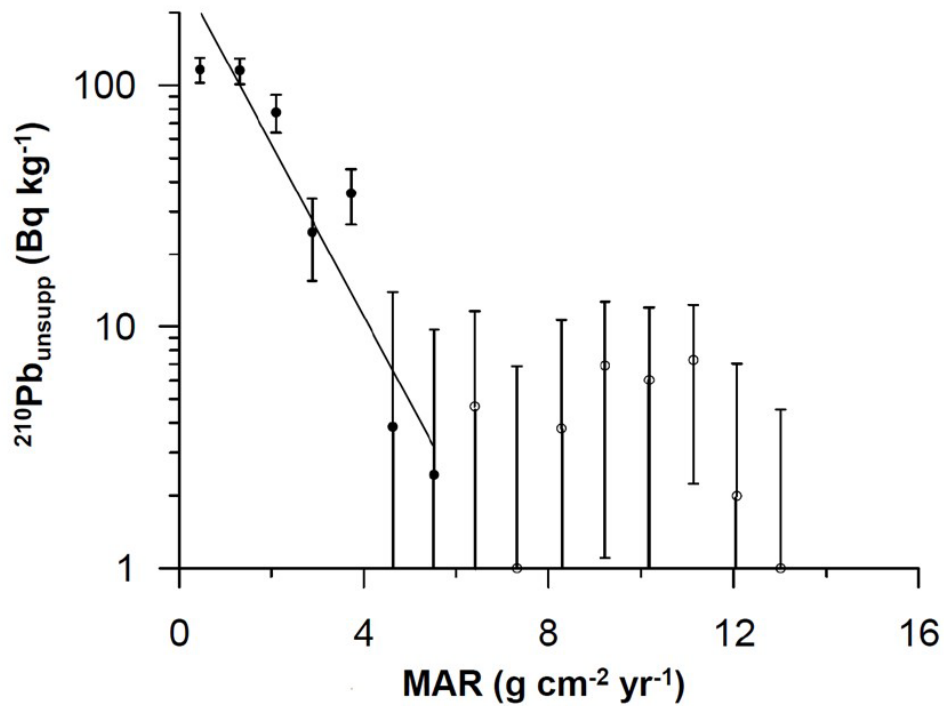
indicating the maximum and minimum ages (Extended Data Table 1). The vertical dashed line shows the age of 8.2 kyr BP where the benthic and planktic $\delta^{13}\text{C}$ records of the two cores were spliced in Figure 2a and 2b (i.e. only $\delta^{13}\text{C}$ data from below 230 cm depth were used from core PS75/167-1 and only $\delta^{13}\text{C}$ data from above 380 cm depth were used from core PS75/160-1).



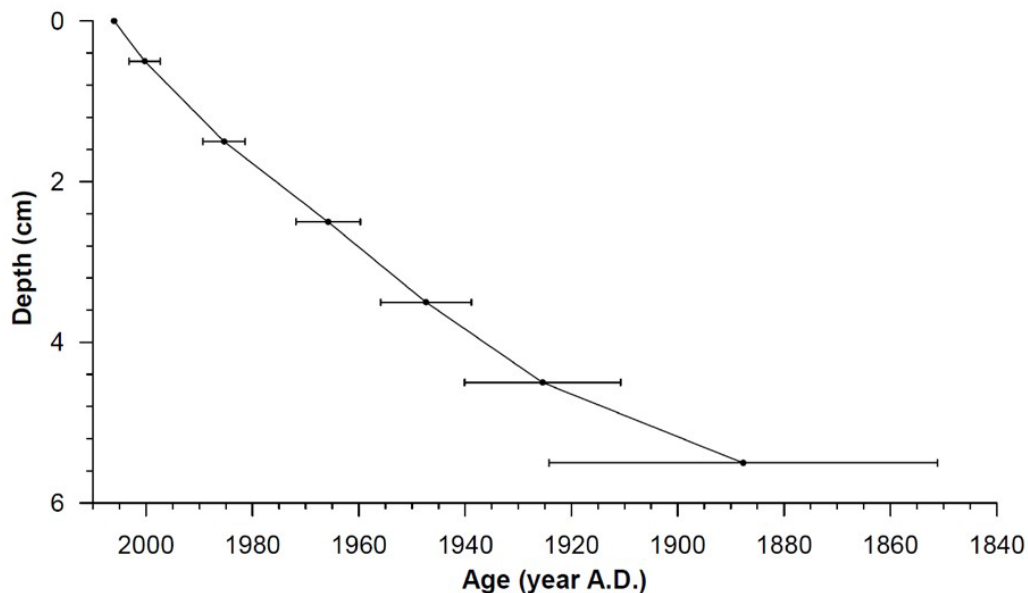
Extended Data Figure 2: Concentrations of radiogenic lead and caesium isotope concentrations versus depth in giant box core PS69/251-1.

Left: Concentration of unsupported ^{210}Pb ($^{210}\text{Pb}_{\text{xs}}$). Note logarithmic scale. Surface concentration is $\sim 115 \text{ Bq kg}^{-1}$, and an exponential decline of $^{210}\text{Pb}_{\text{xs}}$ with depth is observed in the upper 6 cm. Activity is at the detection limit or lower below 6 cm depth. The calculated $^{210}\text{Pb}_{\text{xs}}$ flux is $100 \text{ Bq m}^{-2} \text{ yr}^{-1}$, which is in reasonable agreement with the expected flux from atmospheric deposition⁵⁶. Error bars denote one standard deviation of $^{210}\text{Pb}_{\text{xs}}$ concentrations.

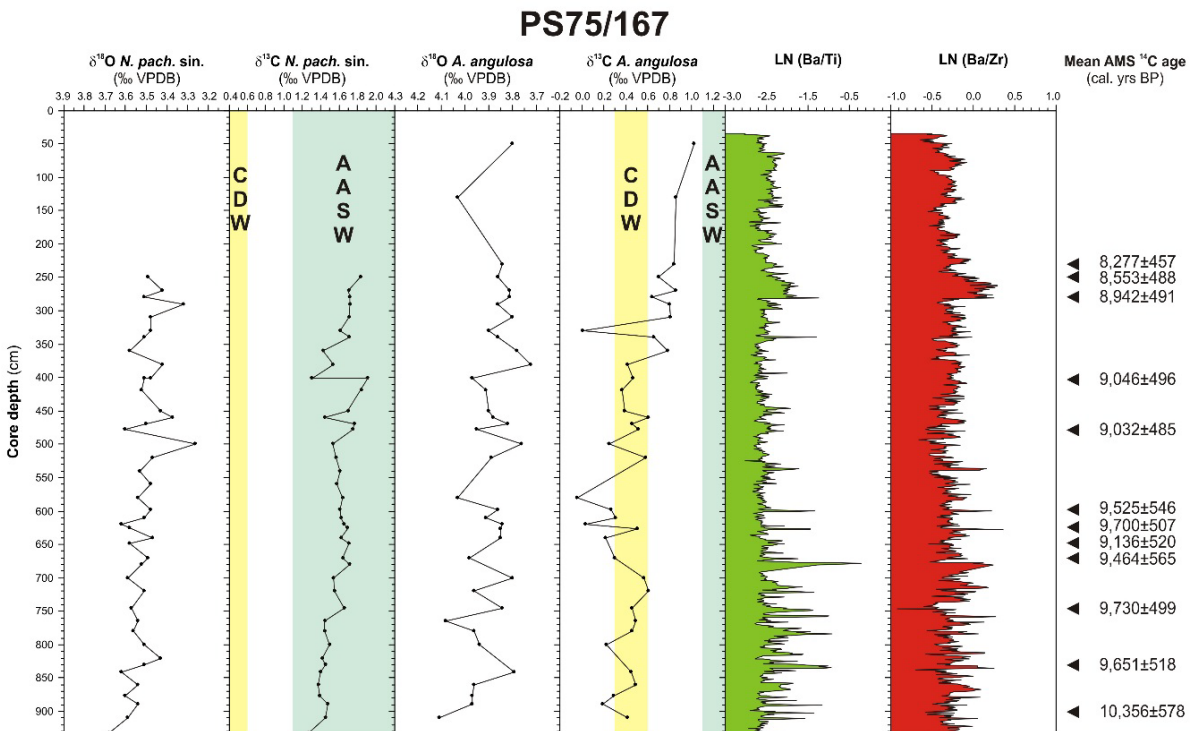
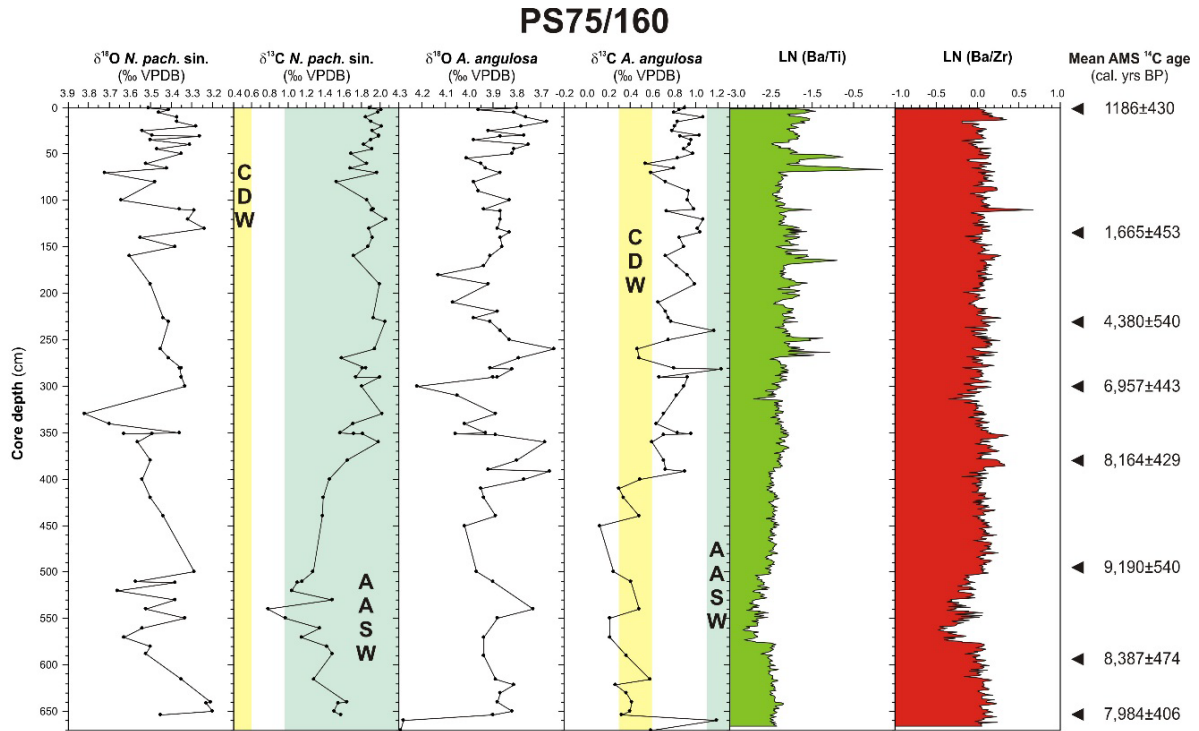
Right: Concentration of ^{137}Cs . Activity is at or below detection limit throughout the core. Error bars denote one standard deviation of ^{137}Cs concentrations.



Extended Data Figure 3: Constant Rate of Supply (CRS) modeling of down-core profile of $^{210}\text{Pb}_{\text{xs}}$ concentrations in core PS69/251-1 using a modified method⁵⁶. Black straight line marks regression to calculate ^{210}Pb concentration below 6 cm core depth. Open circles highlight samples with $^{210}\text{Pb}_{\text{xs}}$ concentrations at or below detection limit. Error bars denote one standard deviation of $^{210}\text{Pb}_{\text{xs}}$ concentrations.

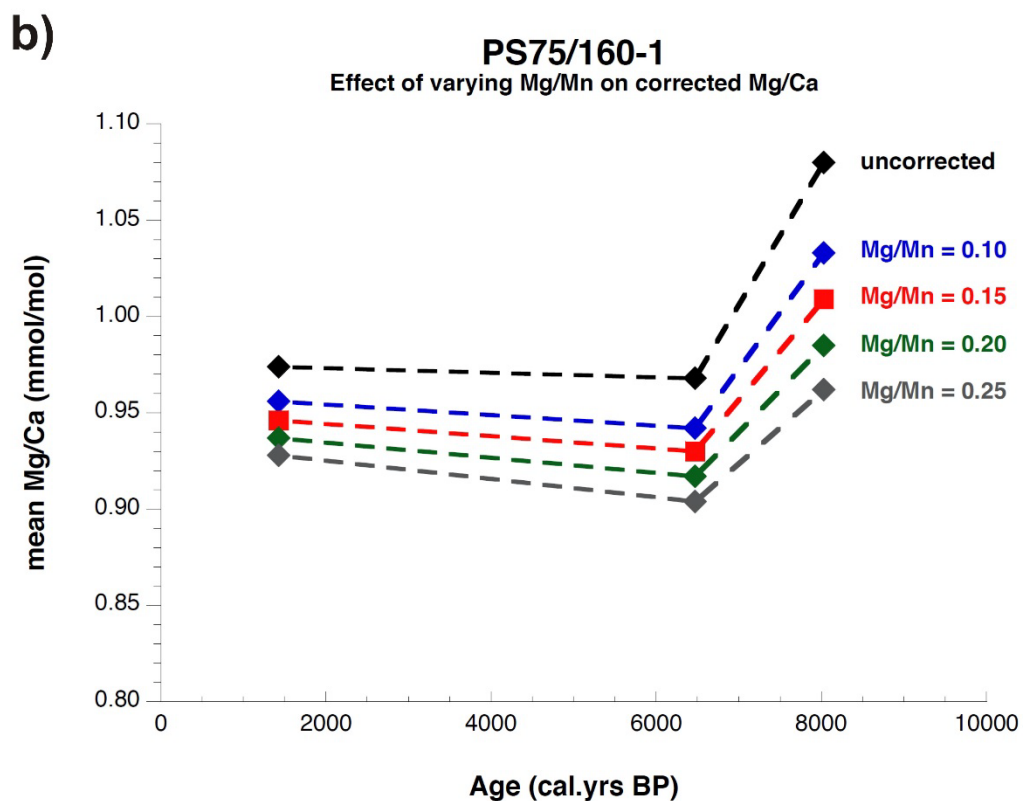
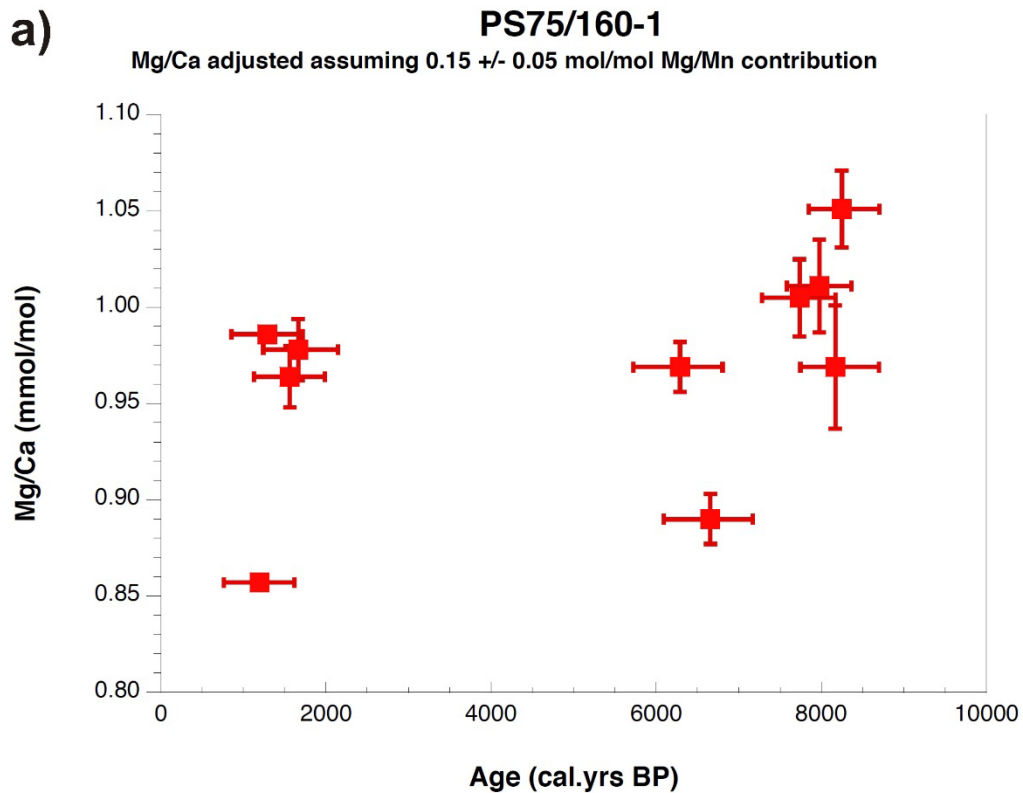


Extended Data Figure 4: Age-depth plot for the upper 5.5 cm of core PS69/251-1 based on CRS modeling of $^{210}\text{Pb}_{\text{xs}}$ concentrations. Error bars denote one standard deviation of calculated ages.



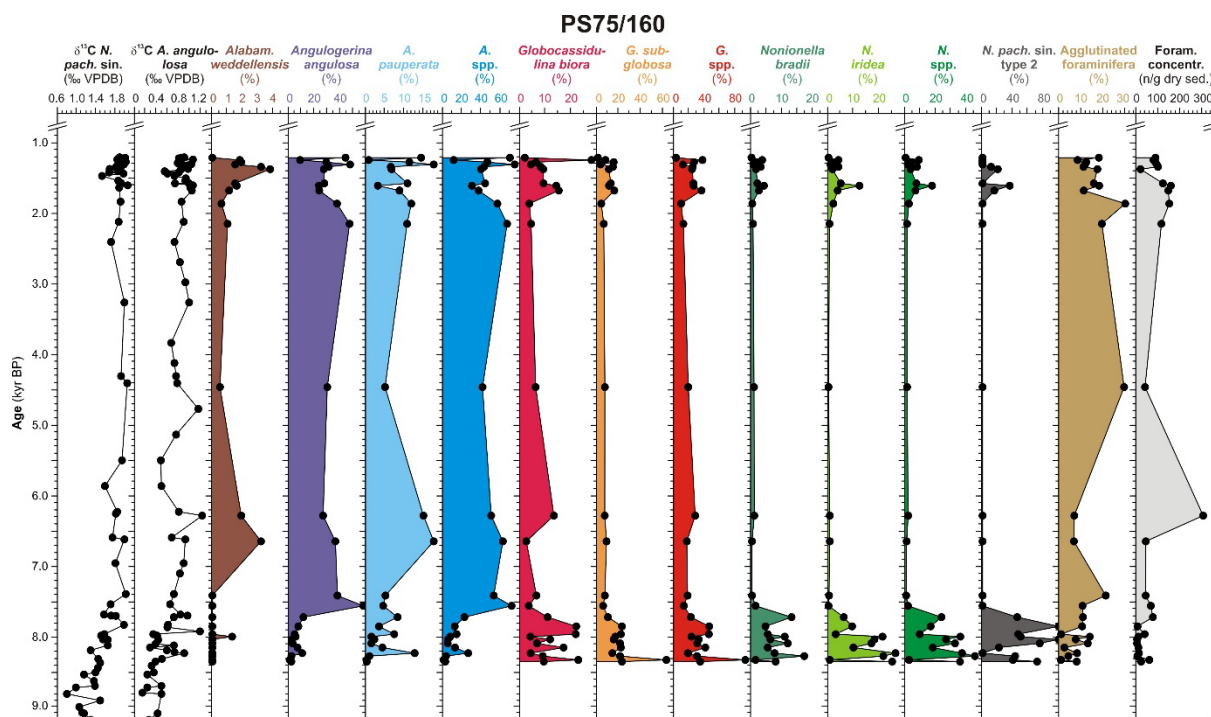
Extended Data Figure 5: Down-core plots of $\delta^{18}\text{O}$ and $\delta^{13}\text{C}$ isotope ratios measured on planktic (*Neogloboquadrina pachyderma* sinistral) and benthic foraminifera (*Angulogerina angulosa*), LN(Ba/Ti), LN(Ba/Zr) and AMS ^{14}C ages of calcareous microfossils^{21,22,53} of cores PS75/160-1 (above) and PS75/167-1 (below). The ranges of $\delta^{13}\text{C}$ values typical for AASW and CDW are indicated by the blue-green and yellow shaded areas,

respectively. While prominent peaks in LN(Ba/Ti) below ~220 cm core depth in core PS75/167-1 are significantly higher than the background LN(Ba/Ti) values, the LN(Ba/Zr) peaks are not significantly higher in this core section. This relation suggests that the LN(Ba/Ti) and Ba/Ti peaks are caused by barium input through increased supply of terrigenous heavy minerals (including barite and zircon), which is confirmed by the down-core increase of terrigenous sand layers below ~220 cm core depth (see Fig. 2 in ref. 21).

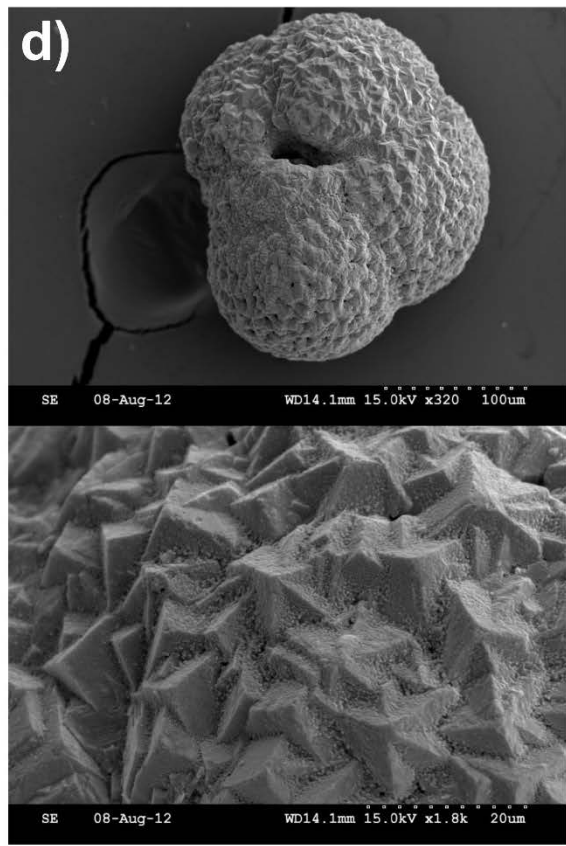
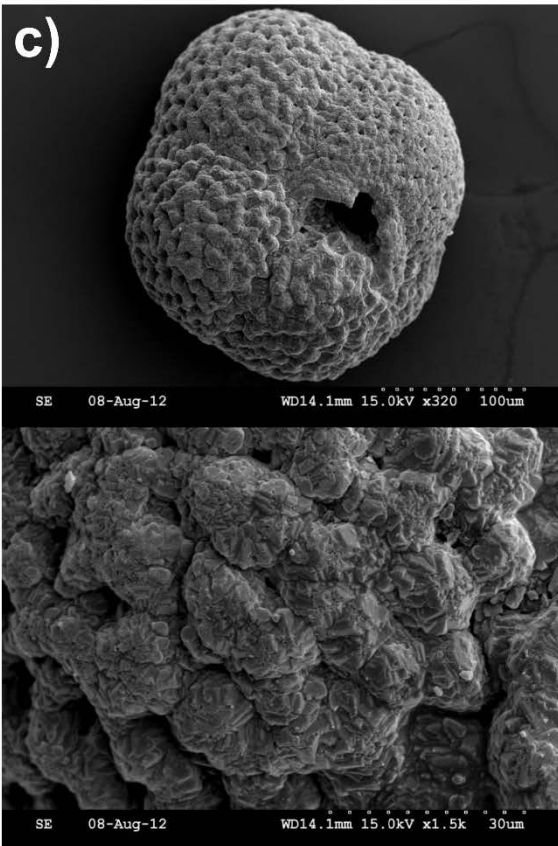
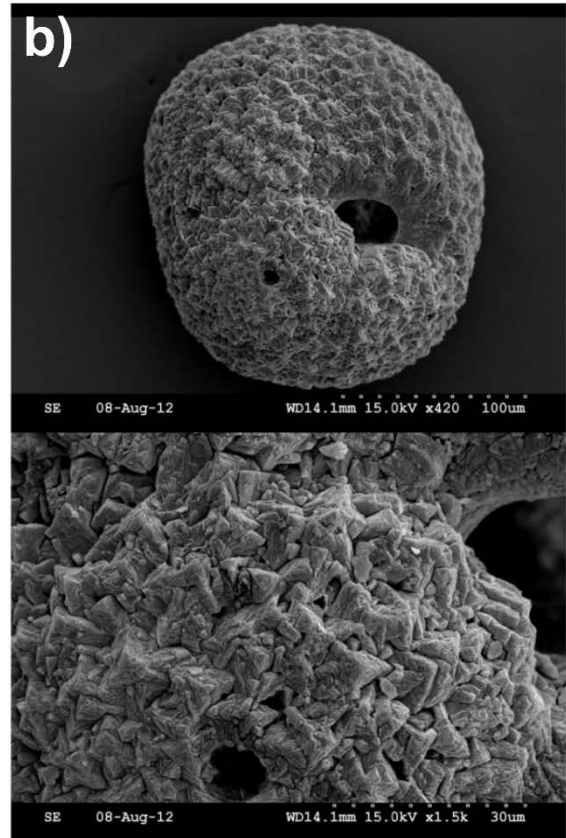
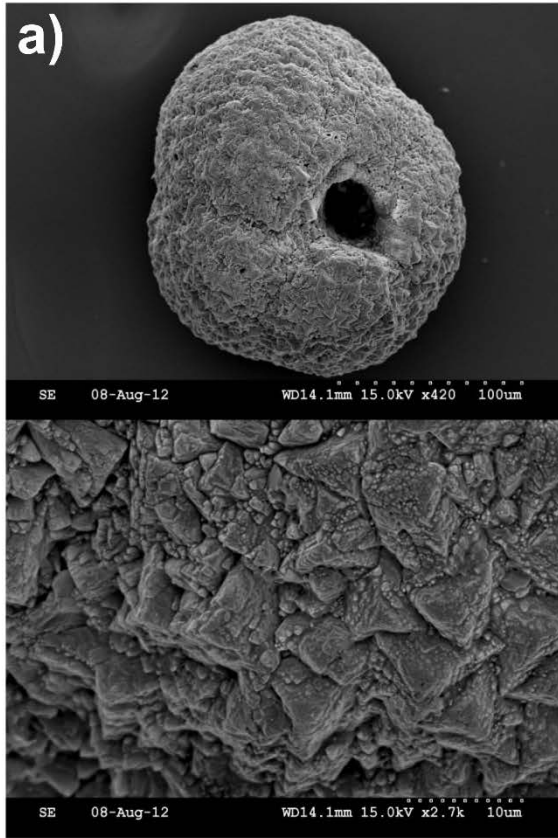


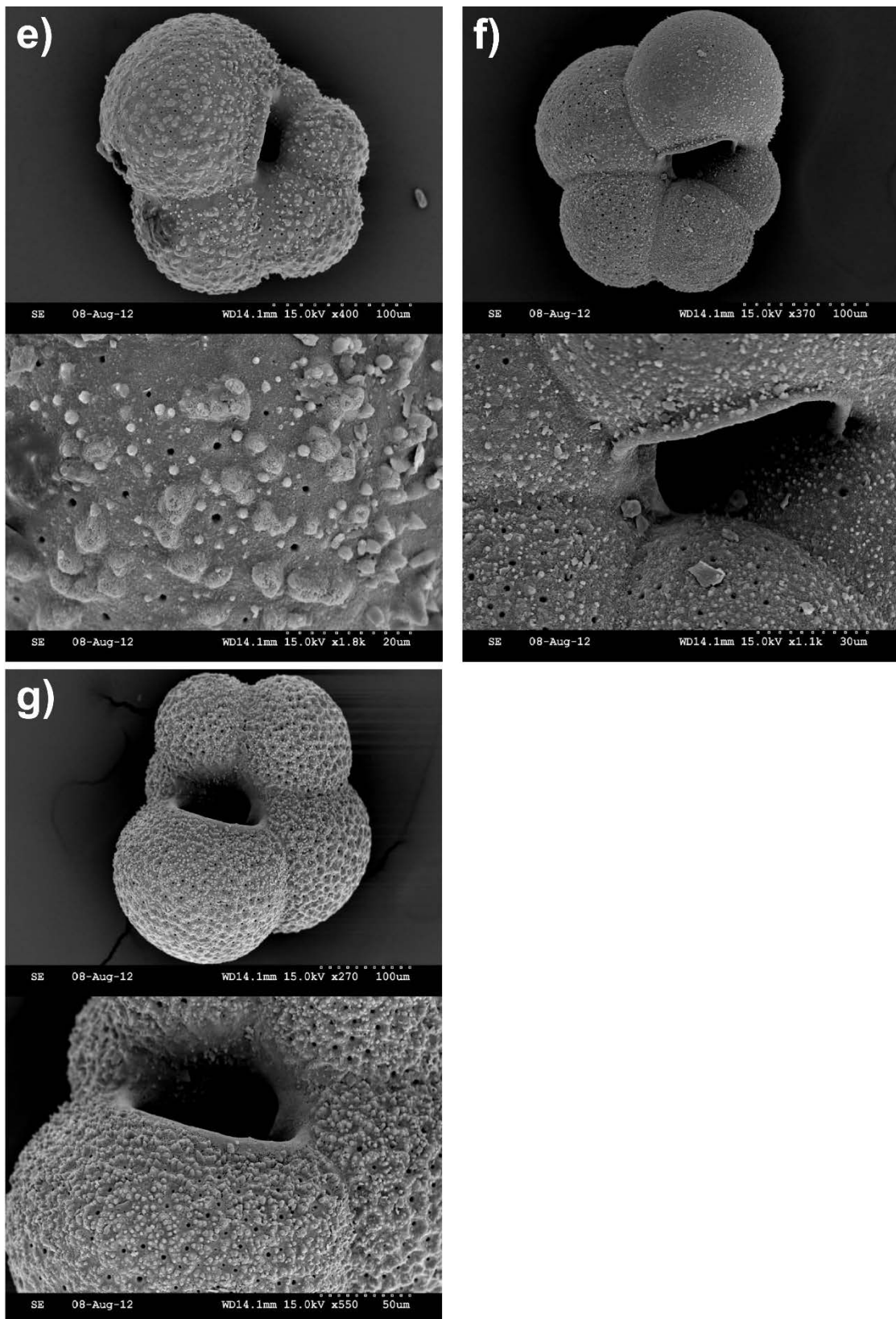
Extended Data Figure 6: Mg/Ca ratios of benthic foraminifer shells (*A. angulosa*) in core PS75/160-1 adjusted for a potential diagenetic Mg contribution by assuming the Mg/Mn ratio of a diagenetic coating is 0.15 ± 0.05 mol/mol (Extended Data Figure 6a), and

displayed as sample groups with ages of 10.0-7.5 kyr BP (4 samples), 7.5-4.0 kyr BP (2 samples) and 4.0-0 kyr BP (4 samples) with no adjustment and adjusted for potential diagenetic Mg contributions and Mg/Mn ratios in diagenetic coatings of 0.10, 0.15, 0.20 and 0.25 (Extended Data Figure 6b; references 68-72). Error bars in Extended Data Figure 6a result from the uncertainty of ± 0.05 mol/mol for the Mg/Mn composition of the coating and the range of the calibrated AMS ^{14}C dates of neighbouring sample horizons (Extended Data Table 1), from which the ages for the Mg/Ca samples were calculated.



Extended Data Figure 7: Holocene changes in foraminifer assemblages of core PS75/160-1 from Pine Island Bay. Benthic foraminifer assemblages (only the most abundant and selected benthic taxa are displayed), abundance of *N. pachyderma* sin. type 2 in relation to all foraminifera, abundance of arenaceous benthic foraminifera (in relation to all benthic foraminifera) and total foraminifer concentration (individuals per gram dry sediment). $\delta^{13}\text{C}$ composition of planktic and benthic foraminifera is also shown. Note major shift in foraminifer abundances and assemblages centred at 7.5 kyr BP. Benthic foraminifer taxa: *Alabaminella weddellensis*, *Angulogerina angulosa*, *Angulogerina pauperata*, *Angulogerina* spp. (= sum of all *Angulogerina* species), *Globocassidulina biora*, *Globocassidulina subglobosa*, *Globocassidulina* spp. (= sum of all *Globocassidulina* species), *Nonionella bradii*, *Nonionella iridea*, *Nonionella* spp. (= sum of all *Nonionella* species).





Extended Data Figure 8: Scanning Electron Microscope (SEM) images of whole shells and detailed shell surfaces of *Neogloboquadrina pachyderma* sin. morphotypes 1 and 2 in core PS75/160-1. Morphotype 1 is encrusted with gametogenic calcite and dominates the upper

section of the core (**Extended Data Fig. 8a-d**), while thin-walled and non-encrusted morphotype 2 (**Extended Data Fig. 8e-g**) dominates the lower section of core PS75/160-1. A scale bar (white dots) is shown in the lower right corner of each photo, and the unit of its length (number) is given in μm . Note the indistinct chambers and gametogenic calcite secreted around the whole shell in morphotype 1, while the individual chambers and porous shells of morphotype 2 are clearly visible, thereby showing beginning encrustation (white calcite around pores) (cf. refs. 42, 91-93). Morphotype 1 usually dominates the lower part of the water column in Antarctic and Arctic waters and is preserved in marine sediments, whereas morphotype 2 is abundant in the upper part of the water column and not preserved in the sediments^{42,91-93}. Encrusted morphotype 1 is typical for the terminal life stage of *N. pachyderma* sin., while non-encrusted morphotype 2 is typical for its neanic (i.e. adolescent) to adult stage^{42,91-94}. In analogy with the SEM-defined progressive dissolution steps distinguished by Henrich⁹⁵, **Extended Data Fig. 8a** and **8b** show shells with intermediate dissolution, **Extended Data Fig. 7c** a shell with initial to intermediate dissolution, **Extended Data Fig. 8d** a shell with initial dissolution and **Extended Data Fig. 8e, 8f** and **8g** well preserved shells.

Extended Data Tables

Core ID	Latitude (°S)	Longitude (°W)	Water depth (m)	Recovery (m)	Sample depth (cmbsf)	Laboratory code	Dated mat.	¹⁴ C age ±error (yr BP)	Max. age (yr BP)	Min. age (yr BP)	Med. age (yr BP)	Mean age (yr BP)
PS2544-1 GBC	71.796	105.191	546	0.21	surface	N/A	N/A	N/A	N/A	N/A	N/A	N/A
PS69/251-1 GBC	72.069	104.483	573	0.38	surface	SUERC-18942	pF	1144±37	N/A	N/A	[0]	[0]
PS75/215-1 GBC	74.592	104.042	556	0.62	surface	Beta-315966	Bz	1190±30	N/A	N/A	[0]	[0]
PS75/160-1 GC	74.564	102.624	337	6.68	0.5	Beta-284601	bF, S, O	2340±40	1615	756	1190	1186
					133.5	Beta-284602	S	2750±40	2118	1212	1634	1665
					230	Beta-284604	bF, S, O	4990±40	4919	3840	4405	4380
					300	Beta-284681	bF, S	7180±40	7400	6514	6967	6957
					380	Beta-284606	bF, S	8410±40	8592	7735	8137	8164
					490+500	Beta-284607	bF, P, S, O	9320±40	9729	8650	9243	9190
					588+600	Beta-284608	bF, S, O, Bp	8560±40	8861	7913	8331	8387
					652	Beta-284610	S	8200±40	8358	7578	7966	7968
					top of CC	Beta-284600	Bp, S, bF	8240±40	8390	7603	8006	7997
PS75/167-1 GC	74.623	105.802	526	9.34	230	Beta-300838	F	8490±40	8734	7820	8254	8277
					250	Beta-300839	F, S	8740±40	9040	8065	8547	8553
					280	Beta-284682	F	9080±50	9432	8451	8949	8942
					401	Beta-284683	F, S, O	9210±50	9541	8550	9113	9046
					478	Beta-300837	F, O, E	9180±40	9516	8547	9077	9032
					598	Beta-300840	F	9490±40	10070	8979	9459	9525
					625.5	Beta-284684	F	9660±50	10206	9193	9690	9700
					649	Beta-300841	F	9280±40	9656	8616	9196	9136
					670	Beta-284685	F	9450±50	10029	8899	9405	9464
					746	Beta-284686	F, S	9690±50	10228	9231	9726	9730
					830	Beta-300842	F	9620±50	10169	9133	9640	9651
					900.5	Beta-284687	F, S	10210±60	10934	9778	10372	10356

Extended Data Table 1: Locations, conventional and calibrated AMS ^{14}C dates on calcareous microfossils from the investigated sediment cores. Coring devices: GBC: giant box core, GC: gravity core. Sample depths are given in centimetres below seafloor (cmbsf; top of CC: sample was taken from top of core catcher, corresponding to 652 cmbsf). All ^{14}C -dates were corrected using an offset (ΔR) of 700 ± 200 years from the global marine reservoir effect (R) of 400 years. The corrected ^{14}C -dates were calibrated with the CALIB Radiocarbon Calibration Program version 7.1html⁵⁴ (<http://calib.qub.ac.uk/calib/>) using the MARINE13 calibration dataset⁵⁵. Uncorrected dates ($=^{14}\text{C}$ age) are given in ^{14}C years before present (BP) and maximum, minimum, median and mean dates are given in calibrated years BP. Errors of calibrated dates are given as a 2σ range. Dated calcareous microfossils: bF: benthic foraminifera, Bp: brachiopods, Bz: bryozoans, E: echinoid spines, F: mixed benthic and planktonic foraminifera, O: ostracods, P: pteropods, pF: planktonic foraminifera, S: unspecified calcareous shell fragments.

1

Depth (cm)	Age (yr)	Age error (yr)	Date (yr AD)	Mass accumulation rate (kg m ⁻² yr ⁻¹)	Mass accumulation rate error (kg m ⁻² yr ⁻¹)
0			2006		
0-1	6	3	2000	0.78	0.10
1-2	21	4	1985	0.57	0.10
2-3	40	6	1966	0.41	0.10
3-4	59	9	1947	0.42	0.16
4-5	81	15	1925	0.38	0.19
5-6	118	37	1888	0.24	0.28

2

3 **Extended Data Table 2: Chronology of the upper 6 cm of core PS69/251-1 based**
4 **on CRS-modeling of ²¹⁰Pb_{xs} concentrations.**

5

6

7 SUPPLEMENTARY REFERENCES

- 8 51. Gohl, K. (ed.), *The expedition of the Research Vessel "Polarstern" to the*
9 *Amundsen Sea, Antarctica. 2010 (ANT-XXVI/3), Repts. Polar Mar. Res. 617,*
10 *173 pp. (2010).*
- 11 52. Gohl, K. (ed.), *The expedition ANT-XXIII/4 of the research vessel Polarstern in*
12 *2006, Repts. Polar Mar. Res. 557, 166 pp. (2007).*
- 13 53. Smith, J.A. *et al.* New constraints on the timing of West Antarctic Ice Sheet
14 retreat in the eastern Amundsen Sea since the Last Glacial Maximum. *Global*
15 *Planet. Change 122, 224-237 (2014).*
- 16 54. Stuiver, M. & Reimer, P.J.. Extended ¹⁴C data base and revised CALIB 3.0 ¹⁴C
17 age calibration program. *Radiocarbon 35, 215-230 (1993).*
- 18 55. Reimer, P.J. *et al.* INTCAL13 and MARINE13 radiocarbon age calibration
19 curves 0-50,000 years cal BP. *Radiocarbon 55, 1869-1887 (2013).*
- 20 56. Appleby, P.G. in *Tracking environmental change using lake sediments. Volume*
21 *1: Basin analysis, coring and chronological techniques* (eds. Last, W.M. &
22 Smol, J.P.), Chronostratigraphic techniques in recent sediments, pp. 171-203
23 (Kluwer Academic, Dordrecht, 2001).
- 24 57. Richter, T.O. *et al.* in, *New Techniques in Sediment Core Analysis* (ed.
25 Rothwell, R.G.), The Avaatech XRF Core Scanner: technical description and
26 applications to NE Atlantic sediments, *Geol. Soc. London Special Publ. 267*, pp.
27 39-50 (The Geological Society of London, London, 2006).
- 28 58. Hillenbrand, C.-D., Kuhn, G. & Frederichs, T. Record of a Mid-Pleistocene
29 depositional anomaly in West Antarctic continental margin sediments: an
30 indicator for ice-sheet collapse? *Quat. Sci. Rev. 28, 1147-1159 (2009).*
- 31 59. Nürnberg, C.C., Bohrmann, G. & Schlüter, M. Barium accumulation in the
32 Atlantic sector of the Southern Ocean: results from 190.000-year records.
33 *Paleoceanography 12, 594-603 (1997).*
- 34 60. Jaccard, S.L. *et al.* Two modes of change in Southern Ocean productivity over
35 the past million years. *Science 339, 1419-1423 (2013).*

- 36 61. Weltje, G.J. & Tjallingii, R. Calibration of XRF core scanners for quantitative
37 geochemical logging of sediment cores: Theory and application *Earth Planet.*
38 *Sci. Lett.* **274**, 423-438 (2008).
- 39 62. Barker, S., Greaves, M. & Elderfield, H. A study of cleaning procedures used
40 for foraminiferal Mg/Ca paleothermometry. *Geochem. Geophys. Geosyst.* **4**,
41 8407, doi:10.1029/2003GC000559 (2003).
- 42 63. de Villiers, S., Greaves, M.J. & Elderfield, H. An intensity ratio calibration
43 method for the accurate determination of Mg/Ca and Sr/Ca of marine carbonates
44 by ICP-AES. *Geochem. Geophys. Geosyst.* **3**, GC000169,
45 doi:10.1029/2001GC000169 (2002).
- 46 64. Misra, S. *et al.* Determination of B/Ca of natural carbonates by HR-ICP-MS.
47 *Geochem. Geophys. Geosyst.* **15**, 1617-1628, doi:10.1002/2013GC005049
48 (2014).
- 49 65. Rosenthal, Y. *et al.* Interlaboratory comparison study of Mg/Ca and Sr/Ca
50 measurements in planktonic foraminifera for paleoceanographic research
51 *Geochem. Geophys. Geosyst.* **5**, Q04D09, doi:10.1029/2003GC000650 (2004).
- 52 66. Greaves, M. *et al.* Interlaboratory comparison study of calibration standards for
53 foraminiferal Mg/Ca thermometry. *Geochem. Geophys. Geosyst.* **9**, Q08010,
54 doi:10.1029/2008GC001974 (2008).
- 55 67. Pena, L.D. *et al.* Characterization of contaminant phases in foraminifera
56 carbonates by electron microprobe mapping. *Geochem. Geophys. Geosyst.* **9**,
57 Q07012, doi:10.1029/2008GC002018 (2008).
- 58 68. de Lange, G.J., Van Os, B.J.H. & Poorter, R. Geochemical composition and
59 inferred accretion rates of sediments and manganese nodules from a submarine
60 hill in the Madeira Abyssal Plain, eastern North Atlantic. *Mar. Geol.* **109**, 171-
61 194 (1992).
- 62 69. Hasenfratz, A.P. *et al.* Determination of the Mg/Mn ratio in foraminiferal
63 coatings: An approach to correct Mg/Ca temperatures for Mn-rich contaminant
64 phases. *Earth Planet. Sci. Lett.* **457**, 335-347 (2017).

- 65 70. Hein, J.R. & Koschinsky, A. in *Treatise on Geochemistry* **13** (ed. Scott, S.D.),
66 Deep-Ocean Ferromanganese Crusts and Nodules, pp. 273-291 (Elsevier,
67 Amsterdam, 2014).
- 68 71. Hein, J.R. *et al.* in *Handbook of Ore Mineral Deposits* (ed. Cronan, D.S.),
69 Cobalt-Rich Ferromanganese Crusts in the Pacific, pp. 239-279 (CRC Press,
70 Boca Raton-London-New York-Washington D.C., 1999).
- 71 72. Bolton, B.R., Exon, N.F., Ostwald, J. & Kudrass, H.R. Geochemistry of
72 ferromanganese crusts and nodules from the South Tasman Rise, southeast of
73 Australia. *Mar. Geol.* **84**, 53-80 (1988).
- 74 73. Rickaby, R.E.M., Elderfield, H., Roberts, N., Hillenbrand, C.-D. & Mackensen,
75 A. Evidence for elevated alkalinity in the glacial Southern Ocean.
76 *Paleoceanography* **25**, PA1209, doi:10.1029/2009PA001762 (2010).
- 77 74. Yu, J., Foster, G.L., Elderfield, H., Broecker, W.S. & Clark, E. An evaluation
78 of benthic foraminiferal B/Ca and $\delta^{11}\text{B}$ for deep ocean carbonate ion and pH
79 reconstructions. *Earth Planet. Sci. Lett.* **293**, 114-120 (2010).
- 80 75. Elderfield, H. *et al.* Evolution of ocean temperature and ice volume through the
81 Mid-Pleistocene Climate Transition. *Science* **337**, 704-709 (2012).
- 82 76. Yu, J. & Elderfield, H. Mg/Ca in the benthic foraminifera *Cibicidoides*
83 *wuellerstorfi* and *Cibicidoides mundulus*: Temperature versus carbonate ion
84 saturation. *Earth Planet. Sci. Lett.* **276**, 129-139 (2008).
- 85 77. Yu, J. & Elderfield, H. Benthic foraminiferal B/Ca ratios reflect deep water
86 carbonate saturation state. *Earth Planet. Sci. Lett.* **258**, 73-86 (2007).
- 87 78. Broecker, W.S. & Sutherland, W.S. Distribution of carbonate ion in the deep
88 ocean: Support for a post-Little Ice Age change in Southern Ocean ventilation?
89 *Geochem. Geophys. Geosyst.* **1**, 1023, doi:10.1029/2000GC000039 (2000).
- 90 79. Duplessy, J.C., Roche, D.M. & Kageyama, M. The deep ocean during the last
91 interglacial period. *Science* **316**, 89-91 (2007).
- 92 80. Piotrowski, A.P., Goldstein, S.L., Hemming, S.R. & Fairbanks, R.G. Temporal
93 relationships of carbon cycling and ocean circulation at glacial boundaries.
94 *Science* **307**, 1933-1938 (2005).

- 95 81. Curry, W.B. & Oppo, D.W. Glacial water mass geometry and the distribution
96 of $\delta^{13}\text{C}$ of ΣCO_2 in the western Atlantic Ocean. *Paleoceanography* **20**, PA1017,
97 doi:10.1029/2004PA001021 (2005).
- 98 82. Poole, C. *Did ice shelf cover for inner Pine Island Bay (Amundsen Sea, West*
99 *Antarctica) persist until the latest Holocene?* 83 pp. (MGeol thesis, Department
100 of Geology, University of Leicester, UK, 2012).
- 101 83. Mackensen, A., Grobe, H., Kuhn, G. & Fütterer, D.K. Benthic foraminiferal
102 assemblages from the eastern Weddell Sea between 68 and 73°S: Distribution,
103 ecology and fossilization potential. *Marine Micropal.* **16**, 241-283 (1990).
- 104 84. Murray, J.W. & Pudsey, C.J., Living (stained) and dead foraminifera from the
105 newly ice-free Larsen Ice Shelf, Weddell Sea, Antarctica: ecology and
106 taphonomy\$ *Marine Micropal.* **53**, 67-81 (2004).
- 107 85. Mikhalevich, V.I. The general aspects of the distribution of Antarctic
108 foraminifera. *Micropaleontology* **50**, 179-194 (2004).
- 109 86. Murray, J.W. *An Atlas of British Recent Foraminiferids*. 244 pp (Heinemann,
110 London, 1971).
- 111 87. Murray, J.W. Revised taxonomy, an atlas of British Recent foraminiferids. *J.*
112 *Micropal.* **19**, p. 44 (2000).
- 113 88. Schweizer, M., Pawlowski, J., Duijnste, I.A.P., Kouwenhoven, T.J. & van der
114 Zwaan, G.J. Molecular phylogeny of the foraminiferal genus *Uvigerina* based
115 on ribosomal DNA sequences. *Mar. Micropal.* **57**, 51-67 (2005).
- 116 89. Schweizer, M., Jorissen, F. & Geslin, E. Contributions of molecular
117 phylogenetics to foraminiferal taxonomy: General overview and example of
118 *Pseudoepionides falsobeccarii* Rouvillois, 1974. *Comptes Rendus Palevol.* **10**,
119 95-105 (2011).
- 120 90. Mackensen, A., Schumacher, S., Radke, J. & Schmidt, D.N. Microhabitat
121 preferences and stable carbon isotopes of endobenthic foraminifera: clue to
122 quantitative reconstruction of oceanic new production? *Mar. Micropal.* **40**, 233-
123 258 (2000).

- 124 91. Vilks, G. Comparison of *Globorotalia pachyderma* (Ehrenberg) in the water
125 column and sediments of the Canadian Arctic. *J. Foram. Res.* **5**, 313-325 (1975).
- 126 92. Bergami, C., Capotondi, L., Langone, L., Giglio, F. & Ravaioli, M. Distribution
127 of living planktonic foraminifera in the Ross Sea and the Pacific sector of the
128 Southern Ocean (Antarctica). *Marine Micropal.* **73**, 37-48 (2009).
- 129 93. Kohfeld, K.E., Fairbanks, R.G., Smith, S.L. & Walsh, I.D. *Neogloboquadrina*
130 *pachyderma* (sinistral coiling) as paleoceanographic tracers in polar oceans:
131 Evidence from Northeast Water Polynya plankton tows, sediment traps, and
132 surface sediments. *Paleoceanography* **11**, 679-699 (1996).
- 133 94. Schiebel, R. & Hemleben, C. Modern planktic foraminifera. *Paläontologische*
134 *Zeitschrift* **79**, 135-148 (2005).
- 135 95. Henrich, R. in *Proceedings of the Ocean Drilling Program, Scientific Results*
136 **104** (eds. Eldholm, O., Thiede, J., Taylor E. *et al.*), Glacial/interglacial cycles
137 in the Norwegian Sea: sedimentology, paleoceanography, and evolution of Late
138 Pliocene to Quaternary Northern Hemisphere climate, pp. 189-232 (1989).